



Geometric Quantum Information Structure in Quantum Fields and their Lattice Simulation

Natalie Klco* and Martin J. Savage†

Institute for Nuclear Theory, University of Washington, Seattle, WA 98195-1550, USA

(Dated: August 11, 2020 - 0:45)

Abstract

An upper limit to distillable entanglement between two disconnected regions of massless non-interacting scalar field theory has an exponential decay defined by a geometric decay constant. When regulated at short distances with a spatial lattice, this entanglement abruptly vanishes beyond a dimensionless separation, defining a negativity sphere. In two spatial dimensions, we determine this geometric decay constant between a pair of disks and the growth of the negativity sphere toward the continuum through a series of lattice calculations. Making the connection to quantum field theories in three-spatial dimensions, assuming such quantum information scales appear also in quantum chromodynamics (QCD), a new relative scale may be present in effective field theories describing the low-energy dynamics of nucleons and nuclei. We highlight potential impacts of the distillable entanglement structure on effective field theories, lattice QCD calculations and future quantum simulations.

I. INTRODUCTION

It is well known that the vacuum state of quantum fields exhibits entanglement between spatially separated regions [1–5]. Techniques for extracting this entanglement to auxiliary quantum systems through harvesting and subsequent distillation have been developed for a variety of relativistic fields, in some instances employing accelerating observers to causally disconnect the entanglement detectors [6–10]. This fundamental property of nature may prove useful in the distribution of entangled pairs through local interaction with a background field for quantum communications, sensing, or metrology

as well as in providing new perspectives on the structure of spacetime [11–16].

Recent progress in quantum information has inspired increased consideration of entanglement in high-energy physics and nuclear physics processes. There have been a number of earlier studies examining the role of entanglement in dynamical processes related to high-energy quantum chromodynamics (QCD), such as fragmentation [17–19], heavy-ion collisions [20–23], deep inelastic scattering [24, 25] and even suggestive hints extracted from experimental data [26]. Further, some exciting results have recently been obtained connecting entanglement to emergent symmetries of QCD [27, 28] and to the structure of nuclei [29–31].

In this work, we calculate the geometric constant determining the exponential component of the decay of negativity in the two-dimensional non-interacting massless scalar field vacuum. We further explore the structure of entanglement in the lattice-regulated

* klcon@uw.edu; Affiliation after September 2020:
Institute for Quantum Information and Matter and
Walter Burke Institute for Theoretical Physics,
California Institute of Technology, Pasadena CA
91125, USA

† mjs5@uw.edu

field to inform the design of quantum and classical calculations of quantum coherent observables.

The choice of scalar field is inspired by its simplicity, ubiquity, unique status of having a thoroughly examined qubit digitization [32–36], and having been proven to be BQP complete [37]. The latter of these motivating factors indicates that any efficient quantum calculation, of fields or otherwise, can be transformed with polynomial resources to a scattering process of the interacting scalar field through the manipulation of classical external sources. As such, the entanglement structures found in the dynamical interacting scalar field are expected to be sufficient for the hardware implementation of efficient quantum computations. Perhaps surprisingly considering the naïve simplicity of the massless scalar field, an analytic calculation through conformal field theory of the entanglement structure between disjoint sub-regions even within one spatial dimension remains elusive, complicated in part by its spectroscopic nature with respect to field correlators. However, progress has developed through formidable analytic and high precision numerical investigations of the entanglement structure of the scalar field both in the continuum and using a spatial lattice (harmonic chains) [38–50].

In the following, numerical results in the two dimensional scalar field will be used to motivate discussions related to lattice quantum chromodynamics (LQCD) calculations [51–55] and low-energy effective field theories (EFTs) describing nuclear forces and other confining strongly-interacting theories. Additional calculations in three dimensions are required to make quantitative predictions for previously unknown nonperturbative systematic errors in LQCD calculations, e.g. Refs. [56–59], and for potential impacts in nuclear EFTs, e.g. Refs. [60–64].

In order to quantify entanglement, the logarithmic negativity [65–68] between spatially separated regions of the field is cal-

culated. The negativity—the sum of negative eigenvalues in the partially transposed reduced density matrix—quantifies violation of the parity symmetry in conjugate momentum space that would otherwise be exact in a tensor product state [68]. As a necessary but insufficient separability criterion, the negativity does not capture all quantum correlations [69], though it does provide an upper bound¹ to the distillable entanglement [67, 72].

It has previously been observed that the negativity between individual oscillators of the latticized position-space scalar field vanish beyond nearest neighbor [39–42, 44, 46–50, 73]. This phenomenon is analogous to ESD (entanglement sudden death or early-stage disentanglement) observed in the presence of quantum noise [74–77], where tracing of the scalar lattice external to the regions of interest provides the mechanism of decoherence. While the individual field operators, $\hat{\phi}$ and $\hat{\pi}$, do not produce entanglement at long distances, individual creation/annihilation operators for position space oscillators are sensitive to entanglement at long distances. The translation between these two bases involves a smearing in the field conjugate momentum space and points to the importance of such systematic delocalization for reproducing infrared entanglement properties through a lattice regularization. Naturally, higher resolution of physically separated field regions through a smaller lattice spacing improves agreement with continuum symmetries [78]. Though expected to systematically remove artifacts associated with finite lattice spacing, it is here found that finite negativity *spheres* are not perturbatively removed or expanded through Symanzik improvement [79]

¹ As an upper bound, the exponentially decaying negativity calculated in the continuum massless scalar field does not preclude the possibility that the distillable entanglement of the field is zero. Calculations harvesting entanglement from the scalar field suggest this is not the case [10, 70, 71].

of the lattice dispersion relation. Supporting entangled regions of a latticized field demands a minimum information complexity of the field representation in the regions of interest, with a lattice spacing threshold only below which negativity spheres of sufficient size and accuracy are supported.

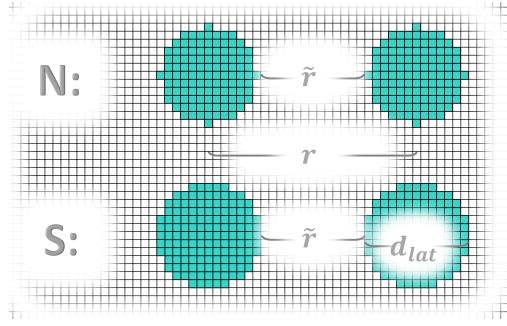


FIG. 1. Two choices of pixelation producing circular regions in the continuum.

Consider circular regions of a 2D massless scalar field discretized onto a lattice (see Fig. 1). In the following, the negativity between the field degrees of freedom within such regions with increased spatial separation is quantified. As conformal theories are without an intrinsic length scale, allowing calculations to be organized by relative dimensions in the continuum, all separations can be expressed in units of the region diameters e.g., \tilde{r}/d . The tilde will be used to indicate a measurement of separation between the region surfaces rather than the distance between region centers. The choice of region diameter as a reference scale allows for a natural transition when considering the nucleon radius to set the scale for the field regions of interest in calculations of QCD. At finite lattice spacing, the continuum limit can be approached in an arbitrary number of ways. Two different pixelations of the regions are shown in Fig. 1. The method labeled “N” begins with a central scalar field site and incorporates all sites within a specified integer radial distance. Organizing these sites into groups by the magnitude of their vector of center displacement integers, $|\mathbf{n}|^2$ [80], the N

boundary is defined with an integer truncation of $|\mathbf{n}|$. The method labeled “S” incorporates additional $|\mathbf{n}|^2$ -shells, truncating $|\mathbf{n}|$ at the next half integer. While the S boundary approaches the continuum more rapidly, the independent perspectives provided by these two trajectories toward the continuum are found to be a valuable quantifier of systematic uncertainties. Calculating the negativity between these field regions determines a fundamental property of the field, the distillable entanglement present within the vacuum. A further application of this information to the operational feasibility of harvesting the present entanglement requires defining a detector structure and coupling to the studied field regions.

For a free non-interacting scalar field, all observables are expressible in terms of two-point vacuum expectation values of the field, $\hat{\phi}$, and conjugate momentum, $\hat{\pi}$, operators. In a finite volume with spatial extent L in each direction and a lattice spacing set equal to one, these two-point functions are,

$$\langle \hat{\chi}(0)\hat{\chi}(\mathbf{r}) \rangle = \sum_{\mathbf{p}} \frac{e^{i\mathbf{p}\cdot\mathbf{r}}}{2L^D} \left(m^2 + \sum_i 4 \sin^2 \left(\frac{p_i}{2} \right) \right)^{\frac{\alpha}{2}}, \quad (1)$$

where $\alpha = 1$ for $\hat{\chi} = \hat{\pi}$, $\alpha = -1$ for $\hat{\chi} = \hat{\phi}$, and \mathbf{r} is a vector of integers. The discrete vector sum over momentum modes incorporates each spatial component taking values in the set $p_i e^{\frac{2\pi}{L}} \mathbb{Z}_L$ with \mathbb{Z}_L a bounded set of integers between 0 and $(L-1)$. While it is possible to calculate entanglement properties between two separated regions through analytic Gaussian integration of the field outside the regions to generate a reduced density operator [38, 73], it is advantageous to instead use expectation values in the thermodynamic limit, $L \rightarrow \infty$, and properties of the symplectic spectrum to represent the calculation of entanglement with only propagators between the two regions [42, 81]. In this case, the log-

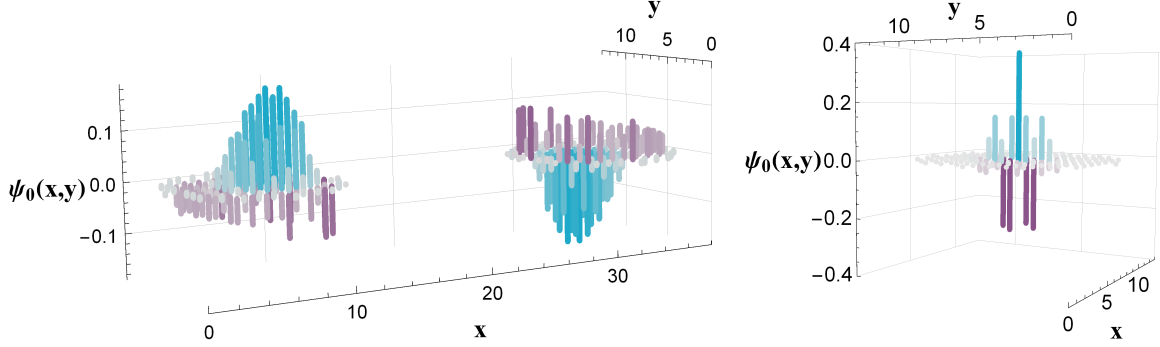


FIG. 2. (left) The ground state wavefunction of the operator product GH^Γ isolated to circular regions of $d_{lat} = 13$ lattice sites across with the N-type boundary shown in Fig. 1. (right) The ground state wavefunction of one isolated region calculated with $\tilde{r} = 100$, a separation beyond the negativity sphere, \tilde{r}_N . Depicted numerical values can be found in Tables I and II of Appendix A.

arithmic negativity can be written as,

$$\mathcal{N} = - \sum_i \log_2 \min(2\sqrt{\lambda_i}, 1) , \quad (2)$$

where the λ_i are eigenvalues of the matrix product GH^Γ with $G_{xy} = \langle \hat{\phi}(x)\hat{\phi}(y) \rangle$, $H_{xy} = \langle \hat{\pi}(x)\hat{\pi}(y) \rangle$, and Γ indicates the partial transposition of H . Though not hermitian, the product GH^Γ enjoys real eigenvalues associated with the symmetric positive definiteness of G and H^Γ . For interacting theories, in which higher-body correlation functions carry distinct information, this Gaussian approximation calculated from propagators alone is expected to provide a lower bound on the logarithmic negativity of the field [82]. For this continuous variable system, the partial transposition of H can be implemented with a reflection in conjugate momentum space of the second region, $\pi_2 \rightarrow -\pi_2$ [68]. In the infinite volume limit (and continuous momentum within the first Brillouin zone) of two-dimensional space, the two-point correlation functions populating G and H can be simplified to,

$$\begin{aligned} \langle \hat{\chi}(0,0)\hat{\chi}(x,y) \rangle = \\ \int_0^\pi dp \frac{(6 - 2 \cos p)^{\frac{\alpha}{2}} \cos yp}{2\pi} \\ {}_3F_2 \left(\begin{matrix} -\alpha/2, 1/2, 1; \\ 1-x, 1+x; \end{matrix} \frac{2}{3-\cos p} \right) , \quad (3) \end{aligned}$$

where ${}_3F_2$ is the regularized hypergeometric function. No infrared regulation is required in two dimensions, allowing the mass to be set to zero ². In this formulation, with oscillatory integrands of increasing frequency and exponentially decreasing eigenvalues of the product GH^Γ in the separation, along with increasing dimensionality of G and H in the lattice spacing, the calculation of the negativity exhibits a sign problem. As such, high-precision is required (typically quadruple precision or greater) for evaluations of the G, H integrals and the following eigenvalue determination, limiting the granularity of achievable region pixelations.

While the point-to-point propagators can be used directly as a basis for G and H , it is convenient to form combinations that reflect the underlying symmetry of the pixelated regions: (1) the reflection symmetry in the plane along their separation axes and (2) the perpendicular reflection plane at the midpoint of their separation. This leads to a block diagonalization of GH^Γ into the symmetry sectors of the parity operators (which

² Massive theories will exhibit additional exponential suppression of the negativity controlled by the mass of the lightest particle. The massless limit has been chosen to isolate the purely geometric contribution.

remain dense matrices). The negativity is dominated (by orders of magnitude at modest separation) by the lowest eigenvalue in the sector of (+,-) parity for reflection planes (1, 2) described above. The wavefunction of this ground state of the product GH^Γ is shown in the left panel of Fig. 2 for configuration $d_{lat} = \tilde{r} = 13$. At a separation equal to one region diameter, this configuration is within the negativity sphere. The wavefunction shows that amplitudes experience an attractive interaction between the two regions, suggestive of a “flux-tube” between them. With respect to the irreps of the dihedral group D_4 , expressing a valid symmetry for individual regions and thus for a region at infinite separation, it is found that isolated contributions to the negativity are organized in the hierarchy of (E, A_1, B_1, A_2, B_2) with the E sector dominant at modest separations beyond the detector size. At separations beyond the negativity spheres, this apparent flux tube is broken and the wavefunction of a region appears as in the right panel of Fig. 2, calculated for $\tilde{r} = 100$. The local horizontal asymmetry of each spatial region in the ground-state wavefunction rapidly decays and the wavefunction acquires approximately an oscillatory Gaussian envelope. In the continuum limit at infinite separation, these regions carry zero “charge” ³.

The results of computing the logarithmic negativity between these circular regions are shown in the left panel of Fig. 3. In the continuum limit, the logarithmic negativity decay is dominated by an exponential with the separation measured in units of the region size, \tilde{r}/d , where d is the diameter across the region and \tilde{r} is the separation between the regions, $\mathcal{N} \sim r^\alpha e^{-\beta \frac{\tilde{r}}{d}}$. Considering only the exponential behavior and not the sub-

leading power-law ⁴, this behavior is controlled by a pure number extrapolated in the second and third panels of Fig. 3 to be $\beta_{2D} = 5.29(4)$ in two dimensions. In the second panel, the reference length scale associated with the regions, d , was chosen to be the largest extent of the circular region along the lattice axis (for the example regions of Fig. 1, $d_{lat} = 13$). This classification places the S and N boundary structures on different trajectories toward the continuum limit of rotationally symmetric field regions. In the third panel of Fig. 3, the reference length scale associated with the field region was chosen to be an averaged diameter calculated from each point on the boundary (for the $d_{lat} = 13$ example regions of Fig. 1, the S boundary has $d_{avg} = 12.36$ while the N boundary has $d_{avg} = 11.27$). This classification connects the trajectories of the S and N boundary structures. The extrapolated entanglement mass, β_{2D} , is consistent between these two diameter definitions, though the latter is found to produce negativity within 1% of the continuum value at larger lattice spacing, as expected for a continuum-inspired spatial averaging. The resulting value of β_{2D} is distinct from that previously calculated in one dimension, $\beta_{1D} = 2.82(3)$ [42], indicating a more rapid decay of distillable entanglement within the massless scalar vacuum in higher dimensional space. It is expected, and the subject of future work, that β_{3D} will be further suppressed.

The existence of a pure number, β , in the massless non-interacting scalar field acting to exponentially suppress quantum correlations in the continuum, as would the presence of a mass scale, presents an opportunity for the appearance of an additional relative scale associated with the geometric entanglement structure in systems without conformal symmetry. With this mechanism, the previous

³ The sum of the amplitudes in the wavefunction of each isolated region vanishes in the continuum.

⁴ The complete functional form will be required for future quantitative estimates of systematic uncertainties in both classical and quantum simulations.

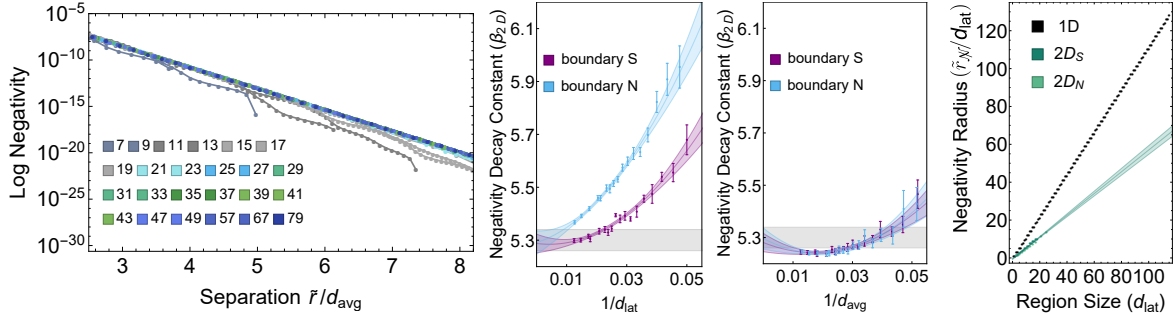


FIG. 3. (left) Logarithmic negativity of two circular regions of the 2D massless non-interacting scalar field as a function of separation distance measured in units of the region diameter (see Fig. 1). Trajectories that end abruptly are found to exhibit zero negativity beyond a finite separation. (middle) Negativity decay constants, β_{2D} , extracted from the decay of logarithmic negativity as a function of the inverse region diameter (lattice spacing in units of the region diameter) extrapolated to zero with two pixelations of the circular field regions. (right) Entanglement sphere radius, $\tilde{r}_{\mathcal{N}}$, as a function of region size in 1D and 2D. Depicted numerical values can be found in Tables III-XIII of Appendix A.

observation of an entanglement-based hierarchy in low-energy nuclear interactions [27], normally predicated on the dominance of local operators, could be understood even without an explicit dimensionful parameter quantifying the entanglement. For example, expecting β_{3D} to be found of similar magnitude to β_{2D} , a rescaling of the radius of the nucleon set by the pion mass with a factor of β empirically produces a mass scale of ~ 350 MeV, a scale found to characterize the convergence of EFT descriptions of nucleon-nucleon interactions when accounting for the characteristic and unjustifiably large scattering lengths [63]. Alternatively, a naïve expectation that $\beta_{3D} \sim 7.7$, approximately linearly extrapolated from $\beta_{1D,2D}$, could indicate an entanglement scale associated with the pion mass to be found around the scale of chiral symmetry breaking. As expected, the numerical results of the two-dimensional massless scalar field are not sufficient to conclusively determine the role played by the negativity decay constant, β , in the design of low-energy effective field theories of the strong interactions. However, these preliminary considerations motivate the non-perturbative computation of β_{3D} in both the scalar field and

QCD, expected to require significant HPC computational resources.

Consistent with an understanding that the lattice representation preferentially captures local properties of the field structure and non-local properties only in the $a \rightarrow 0$ limit, calculations of the negativity at finite lattice spacing non-perturbatively vanish beyond a particular radius, $\tilde{r}_{\mathcal{N}}$. The right panel of Fig. 3 shows the radius of the sphere supporting non-zero negativity, $\tilde{r}_{\mathcal{N}}$, measured in units of the spatial extent of the entangled regions for a 1D and 2D lattice. It is clear that the entanglement radius grows more slowly on a 2D lattice as $\tilde{r}_{\mathcal{N}}/d_{\text{lat}} \sim 0.59(4)d_{\text{lat}}$ compared with that in 1D, $\tilde{r}_{\mathcal{N}}/d_{\text{lat}} \sim 1.118(1)d_{\text{lat}}$. The further constricted negativity sphere radius expected to be found in a 3D geometry warrants exploration of this non-perturbative lattice effect for reliable calculation of coherent quantum phenomena on both classical and quantum computational frameworks.

A non-vanishing lattice spacing introduces features beyond the finite radius negativity sphere. The negativity exhibits an oscillatory component with an amplitude that vanishes in the continuum limit, and falls away from the continuum value as it approaches $\tilde{r}_{\mathcal{N}}$, the

surface of the negativity sphere. These oscillations in negativity introduce an additional systematic error in lattice calculations to be considered, even within $\tilde{r}_{\mathcal{N}}$. For small systems, this can lead to orders of magnitude deviations in the negativity from the continuum limit.

The finite value of $\tilde{r}_{\mathcal{N}}$ implies the existence of a non-perturbative reduction in the physical entanglement volume of a lattice calculation if the observable of interest is sensitive to distillable entanglement. In order to begin understanding the potential implications of the lattice-spacing-induced finite-sized negativity sphere for LQCD calculations, we consider relevant lengths scales in a 2D lattice calculation of two “nucleon-sized” objects interacting through a massless scalar field.

Assuming the nucleon radius is defined by the QCD chiral symmetry breaking scale $r\chi \sim 1/\Lambda_\chi \sim 0.2$ fm, and the scalar field is defined on a 2D grid with a lattice spacing of $a \sim 0.1$ fm (corresponding to $d_\chi \sim 5$ lattice sites across the nucleon), the radius of the negativity sphere is $\tilde{r}_{\mathcal{N}} \sim 0.8$ fm. At this radius, the logarithmic negativity is $\mathcal{N} \sim 10^{-7}$. Therefore, beyond a separation of $r_{\mathcal{N}} \sim 1.2$ fm, the long-distance entanglement structure of the system is incorrect, but only at the level of $\lesssim 10^{-7}$ in the distillable entanglement. A slightly increased lattice spacing of $a = 0.15$ fm corresponds to a vanishing of the logarithmic negativity at $\tilde{r}_{\mathcal{N}} \sim 0.3$ fm, introducing an entanglement error at the 10^{-5} level. If the size of the nucleons is set by the physical pion mass, $r\chi \sim 1/m_\pi \sim 1.4$ fm (corresponding to $d_{m_\pi} \sim 30$ lattice sites across for $a = 0.1$ fm), the negativity sphere has a radius of $\tilde{r}_{\mathcal{N}} \sim 47$ fm with $\mathcal{N} \sim 1 \times 10^{-40}$. In the case of lattice EFT [83–86] with dynamical pions, the death of entanglement is likely of greater significance as lattice spacings tend to be larger than those applied in the estimates above.

These 2D estimates indicate that, for coherent quantum observables, LQCD calculations with coarse lattice spacings and quark

masses that are physical or heavier may vary in their reliability, with these errors exponentially shrinking with lattice spacing or region pixelation. Translating the above observations to LQCD and lattice EFT calculations can only be at a qualitative level without further, *in situ*, numerical investigations in 3D. For LQCD calculations, a much more complex set of estimates are required as the size of the nucleon is dominated by its coupling to pions, which are excitations of the quark condensate, that behave like a fundamental pseudo-scalar field only at low-energies.

However, many classical observables are likely to be insensitive to a lattice truncation of the negativity, as suggested by smooth two-point functions of the field operators and (1×1) -site mutual information calculated in a massive scalar field, reflecting continuum structure with only nearest neighbor (1×1) -site negativity [39–42, 44, 46, 48, 49, 73]. This perspective aligns well with the successes of semi-classical approximations to the structure and interactions of nuclei, including the large- N_c limit of QCD [87–92]. Propagating the impact of the non-perturbative negativity sphere to provide a complete quantification of uncertainties for specifically quantum observables requires further research.

Beyond the 2-body negativity spheres, we anticipate irreducible 3-body negativity spheres involving three spatially separated regions that do not factorize into combinations of 1-body and 2-body negativities. While such irreducibility is well established for qubit systems [93–96], similar quantities remain to be defined in continuous systems of spatially extended field regions.

In LQCD calculations, Luscher’s methods [97–99] have played a central role in extracting physics from finite-volume, Euclidean-space computations. These methods are applicable to simulations on quantum devices with little or no modification, and are expected to play an important role for near-term simulations in small spatial volumes. Finite lattice spacing artifacts are treated as

distinct in LQCD calculations, as they are UV effects, while Luscher’s methods are related to the IR structure of the simulation volume. The impact of the lattice-induced negativity sphere, $\tilde{r}_{\mathcal{N}}$, on finite volume wavefunctions remains to be assessed, though expected to be small for all but quantum coherent observables.

The implications of negativity spheres, $\tilde{r}_{\mathcal{N}}$, in the context of EFTs is interesting to consider further. At the heart of such effective descriptions are multipole expansions. This framework enables the effects of extended sources and sinks in QFTs to be included in low-energy EFTs as local operators ($\delta^{(n)}(\mathbf{r})$, $\delta'^{(n)}(\mathbf{r})$, ...) coupled to the dynamical IR degrees of freedom as in, for example, heavy-baryon chiral perturbation theory [100]. As EFTs require both an operator structure and a prescribed regularization and renormalization scheme, extending the effects of the negativity sphere to the EFT suggests that taking renormalization scales that are disparate from the “size” of the source/sink could lead to discrepancies in the low-energy description of entanglement. This point may be relevant to EFT descriptions of baryons [100] and of nuclear forces [60–64], particularly nucleon-nucleon interactions in channels with a tensor force, which have so far eluded dimensional regularization [101–103] but can be regulated with smearing in either momentum- or position-space. In the case of single baryons, it has been suggested that a spatial regularization would have advantages over massless regularization schemes in the convergence of chiral expansions of baryon properties [104].

In addition to the implications of geometrically-influenced entanglement scales in EFT construction and of negativity spheres in designing latticized calculations of quantum fields, a perspective remains that detailed understanding of UV and IR entanglement properties can be leveraged for computational advantage [73, 105–108]. While the IR physics of interest may be insensitive to specific choices in the UV struc-

ture, demands on computational hardware remain susceptible. The finite negativity sphere at distance $\tilde{r}_{\mathcal{N}}$ scaling inversely with the pixelation of the field region indicates that UV operators (probing length scales of the lattice spacing) cannot access entangled elements of the field at long distances. It is possible that this delocalization may be leveraged to improve robustness of quantum hardware against locally interacting, classically correlated sources of noise when simulating QFTs. Alternatively, designing a field representation with UV entanglement mirroring that found in the IR may provide a reduction in lattice artifacts for coherent quantum observables.

Exploring systematic improvement of the dispersion relation $2 \sin \frac{p_i}{2} \rightarrow p_i$, reveals that the radius of the lattice negativity sphere, $\tilde{r}_{\mathcal{N}}$, and the geometric decay constant, β , are essentially unchanged. Operator and field smearing plays a key role in LQCD calculations, tempering UV fluctuations enabling convergence for low-energy quantities, and mitigating the impact of SO(3) breaking due to the H(3) spatial lattice. We have not performed an extensive study of the impact of field or operator smearing, beyond the dispersion relation, on quantum coherence.

The 2D numerical results provided in this work indicate that the bound on distillable entanglement between two spatially separated regions of the massless non-interacting scalar field vacuum is defined by a decay constant increasing with the dimensionality of spacetime. Viewed as preliminary evidence of similar properties in more complex gauge theories—such as QCD in which a composite (pseudo)scalar field mediates the long-distance interaction between nucleons—the potential impact of this geometric decay constant in providing an entanglement-sensitive scale in the EFT description of nuclei is discussed. When pixelating the regions of interest and latticizing the field for non-perturbative calculation, the distillable entanglement is found to suddenly vanish

at geometrically large separations (relative to the region size) again dependent on the spatial dimension, becoming more artificially localized in higher dimension. A thorough and quantitative understanding of the lattice-induced truncation of the distillable entanglement, from the scalar field to QCD, will be a necessary foundation for the reliable calculation of entangled field excitations as well as their propagation to large distances e.g., when probing real-time coherent fragmentation processes, a central target for quantum simulation. With reduced lattice spacing providing the main source of improvement, the complexity of many-body interactions between collections of lattice sites is determined to be essential for supporting quantum phenomena. The implications of these geometric features of entanglement in quantum fields, on the convergence of low-energy EFTs and the regulation of spatially extended field objects, sheds new light on objectives to non-perturbatively express non-local quantum effects through a hierarchy of local operators and field elements.

plan, Aidan Murran, Caroline Robin, Kenneth Roche, and Alessandro Roggero for valuable discussions. We would also like to thank CENPA at the University of Washington for providing an effective work environment over a period of many months for processing and developing many of the ideas and calculations presented in this paper. Some of this work was performed on the UW’s HYAK High Performance and Data Ecosystem. We have made extensive use of Wolfram Mathematica [109] and the Avanpix multiprecision computing toolbox [110] for MATLAB [111]. NK and MJS were supported by the Institute for Nuclear Theory with DOE grant No. DE-FG02-00ER41132, and Fermi National Accelerator Laboratory PO No. 652197. This work is supported in part by the U.S. Department of Energy, Office of Science, Office of Advanced Scientific Computing Research (ASCR) quantum algorithm teams program, under field work proposal number ERKJ333. NK was supported in part by a Microsoft Research PhD Fellowship.

ACKNOWLEDGMENTS

We would like to thank Silas Beane, Ramya Bhaskar, Joe Carlson, David Ka-

- [1] H. Reeh and S. Schlieder, *Il Nuovo Cimento (1955-1965)* **22**, 1051 (1961).
- [2] S. J. Summers and R. Werner, *Physics Letters A* **110**, 257 (1985).
- [3] S. J. Summers and R. Werner, *Journal of Mathematical Physics* **28**, 2440 (1987), <https://doi.org/10.1063/1.527733>.
- [4] S. J. Summers and R. Werner, *Journal of Mathematical Physics* **28**, 2448 (1987), <https://doi.org/10.1063/1.527734>.
- [5] E. Witten, *Rev. Mod. Phys.* **90**, 045003 (2018), arXiv:1803.04993 [hep-th].
- [6] A. Valentini, *Physics Letters A* **153**, 321 (1991).
- [7] B. Reznik, *Found. Phys.* **33**, 167 (2003), arXiv:quant-ph/0212044.
- [8] B. Reznik, A. Retzker, and J. Silman, *Phys. Rev. A* **71**, 042104 (2005), arXiv:quant-ph/0310058.
- [9] G. Salton, R. B. Mann, and N. C. Menicucci, *New Journal of Physics* **17**, 035001 (2015).
- [10] A. Pozas-Kerstjens and E. Martin-Martinez, *Phys. Rev. D* **92**, 064042 (2015),

- arXiv:1506.03081 [quant-ph].
- [11] S. Ryu and T. Takayanagi, Phys. Rev. Lett. **96**, 181602 (2006), arXiv:hep-th/0603001.
 - [12] S. Ryu and T. Takayanagi, JHEP **08**, 045 (2006), arXiv:hep-th/0605073.
 - [13] G. L. Ver Steeg and N. C. Menicucci, Phys. Rev. D **79**, 044027 (2009), arXiv:0711.3066 [quant-ph].
 - [14] E. Martín-Martínez and N. C. Menicucci, Classical and Quantum Gravity **29**, 224003 (2012).
 - [15] E. Martin-Martinez, A. R. H. Smith, and D. R. Terno, Phys. Rev. D **93**, 044001 (2016), arXiv:1507.02688 [quant-ph].
 - [16] B. Swingle, Annual Review of Condensed Matter Physics **9**, 345 (2018), <https://doi.org/10.1146/annurev-conmatphys-033117-054219>.
 - [17] J. Berges, S. Floerchinger, and R. Venugopalan, Phys. Lett. **B778**, 442 (2018), arXiv:1707.05338 [hep-ph].
 - [18] J. Berges, S. Floerchinger, and R. Venugopalan, JHEP **04**, 145 (2018), arXiv:1712.09362 [hep-th].
 - [19] J. Berges, S. Floerchinger, and R. Venugopalan, *Proceedings, 27th International Conference on Ultrarelativistic Nucleus-Nucleus Collisions (Quark Matter 2018): Venice, Italy, May 14-19, 2018*, Nucl. Phys. **A982**, 819 (2019), arXiv:1812.08120 [hep-th].
 - [20] C. M. Ho and S. D. H. Hsu, Mod. Phys. Lett. **A31**, 1650110 (2016), arXiv:1506.03696 [hep-th].
 - [21] A. Kovner and M. Lublinsky, Phys. Rev. **D92**, 034016 (2015), arXiv:1506.05394 [hep-ph].
 - [22] A. Kovner, M. Lublinsky, and M. Serino, Phys. Lett. **B792**, 4 (2019), arXiv:1806.01089 [hep-ph].
 - [23] N. Armesto, F. Dominguez, A. Kovner, M. Lublinsky, and V. Skokov, JHEP **05**, 025 (2019), arXiv:1901.08080 [hep-ph].
 - [24] D. E. Kharzeev and E. M. Levin, Phys. Rev. **D95**, 114008 (2017), arXiv:1702.03489 [hep-ph].
 - [25] Z. Tu, D. E. Kharzeev, and T. Ullrich, Phys. Rev. Lett. **124**, 062001 (2020), arXiv:1904.11974 [hep-ph].
 - [26] O. K. Baker and D. E. Kharzeev, Phys. Rev. **D98**, 054007 (2018), arXiv:1712.04558 [hep-ph].
 - [27] S. R. Beane, D. B. Kaplan, N. Klco, and M. J. Savage, Phys. Rev. Lett. **122**, 102001 (2019), arXiv:1812.03138 [nucl-th].
 - [28] S. R. Beane and P. Ehlers, Mod. Phys. Lett. A **35**, 2050048 (2019), arXiv:1905.03295 [hep-ph].
 - [29] O. C. Gorton, *Efficient modeling of nuclei through coupling of proton and neutron wavefunctions*, Master's thesis, San Diego State University (2018).
 - [30] O. Gorton and C. W. Johnson, “Entanglement entropy and proton-neutron interactions,” (2019), ESNT workshop on proton-neutron pairing, <http://esnt.cea.fr/Phocea/Page/index.php?id=84>.
 - [31] C. Robin, M. J. Savage, and N. Pillet, (2020), arXiv:2007.09157 [nucl-th].
 - [32] S. P. Jordan, K. S. M. Lee, and J. Preskill, (2011), [Quant. Inf. Comput.14,1014(2014)], arXiv:1112.4833 [hep-th].
 - [33] S. P. Jordan, K. S. M. Lee, and J. Preskill, Science **336**, 1130 (2012), arXiv:1111.3633 [quant-ph].
 - [34] K. Yeter-Aydeniz and G. Siopsis, Phys. Rev. **D97**, 036004 (2018), arXiv:1709.02355 [quant-ph].
 - [35] N. Klco and M. J. Savage, Phys. Rev. **A99**, 052335 (2019), arXiv:1808.10378 [quant-ph].
 - [36] K. Yeter-Aydeniz, E. F. Dumitrescu, A. J. McCaskey, R. S. Bennink, R. C. Pooser, and G. Siopsis, Phys. Rev. A **99**, 032306 (2019).

- [37] S. P. Jordan, H. Krovi, K. S. M. Lee, and J. Preskill, (2017), arXiv:1703.00454 [quant-ph].
- [38] M. Srednicki, Phys. Rev. Lett. **71**, 666 (1993), arXiv:hep-th/9303048 [hep-th].
- [39] K. Audenaert, J. Eisert, M. Plenio, and R. Werner, Phys. Rev. A **66**, 042327 (2002), arXiv:quant-ph/0205025.
- [40] A. Botero and B. Reznik, Physical Review A **70** (2004), 10.1103/physreva.70.052329.
- [41] J. Kofler, V. Vedral, M. S. Kim, and Č. Brukner, Physical Review A **73**, 052107 (2006).
- [42] S. Marcovitch, A. Retzker, M. Plenio, and B. Reznik, Phys. Rev. A **80**, 012325 (2009), arXiv:0811.1288 [quant-ph].
- [43] R. Lohmayer, H. Neuberger, A. Schwimmer, and S. Theisen, Phys. Lett. B **685**, 222 (2010), arXiv:0911.4283 [hep-lat].
- [44] P. Calabrese, J. Cardy, and E. Tonni, J. Stat. Mech. **0911**, P11001 (2009), arXiv:0905.2069 [hep-th].
- [45] H. Casini and M. Huerta, Phys. Lett. B **694**, 167 (2011), arXiv:1007.1813 [hep-th].
- [46] P. Calabrese, J. Cardy, and E. Tonni, Phys. Rev. Lett. **109**, 130502 (2012), arXiv:1206.3092 [cond-mat.stat-mech].
- [47] P. Calabrese, J. Cardy, and E. Tonni, J. Stat. Mech. **1302**, P02008 (2013), arXiv:1210.5359 [cond-mat.stat-mech].
- [48] M. R. Mohammadi Mozaffar and A. Mollabashi, JHEP **07**, 120 (2017), arXiv:1705.00483 [hep-th].
- [49] A. Coser, C. De Nobili, and E. Tonni, Journal of Physics A: Mathematical and Theoretical **50**, 314001 (2017).
- [50] G. Di Giulio and E. Tonni, J. Stat. Mech. **2003**, 033102 (2020), arXiv:1911.07188 [cond-mat.stat-mech].
- [51] H. Politzer, Phys. Rev. Lett. **30**, 1346 (1973).
- [52] D. J. Gross and F. Wilczek, Phys. Rev. Lett. **30**, 1343 (1973).
- [53] K. G. Wilson, Phys. Rev. D **10**, 2445 (1974), [,319(1974)].
- [54] M. Creutz, L. Jacobs, and C. Rebbi, Phys. Rev. Lett. **42**, 1390 (1979).
- [55] R. Balian, J. Drouffe, and C. Itzykson, Phys. Rev. D , 74 (1974).
- [56] [**NPLQCD Collaboration**], S. R. Beane, E. Chang, S. D. Cohen, W. Detmold, H. W. Lin, T. C. Luu, K. Orginos, A. Parreño, M. J. Savage, and A. Walker-Loud, Phys. Rev. **D87**, 34506 (2013), arXiv:1206.5219 [hep-lat].
- [57] S. Aoki, T. Doi, T. Hatsuda, Y. Ikeda, T. Inoue, N. Ishii, K. Murano, H. Nemura, and K. Sasaki (HALQCD), Progress in Theoretical and Experimental Physics **2012**, 01a105 (2012), arXiv:1206.5088 [hep-lat].
- [58] T. Yamazaki, K.-i. Ishikawa, Y. Kuramashi, and A. Ukawa, Phys. Rev. **D92**, 14501 (2015), arXiv:1502.04182 [hep-lat].
- [59] [**NPLQCD**], M. L. Wagman, F. Winter, E. Chang, Z. Davoudi, W. Detmold, K. Orginos, M. J. Savage, and P. E. Shanahan, Phys. Rev. D **96**, 114510 (2017), arXiv:1706.06550 [hep-lat].
- [60] S. Weinberg, Phys. Lett. **B251**, 288 (1990).
- [61] S. Weinberg, Nucl. Phys. **B363**, 3 (1991).
- [62] U. van Kolck, Phys. Rev. C **49**, 2932 (1994).
- [63] D. B. Kaplan, M. J. Savage, and M. B. Wise, Phys. Lett. **B424**, 390 (1998), arXiv:nucl-th/9801034 [nucl-th].
- [64] E. Epelbaum, H. Krebs, and P. Reinert, Front. in Phys. **8**, 98 (2020), arXiv:1911.11875 [nucl-th].

- [65] M. Horodecki, P. Horodecki, and R. Horodecki, Phys. Lett. A **223**, 1 (1996), arXiv:quant-ph/9605038.
- [66] A. Peres, Phys. Rev. Lett. **77**, 1413 (1996), arXiv:quant-ph/9604005.
- [67] G. Vidal and R. Werner, Phys. Rev. A **65**, 032314 (2002), arXiv:quant-ph/0102117.
- [68] R. Simon, Phys. Rev. Lett. **84**, 2726 (2000), arXiv:quant-ph/9909044.
- [69] M. Horodecki, P. Horodecki, and R. Horodecki, Phys. Rev. Lett. **80**, 5239 (1998), arXiv:quant-ph/9801069.
- [70] W. Cong, E. Tjoa, and R. B. Mann, JHEP **06**, 021 (2019), [Erratum: JHEP 07, 051 (2019)], arXiv:1810.07359 [quant-ph].
- [71] L. J. Henderson, A. Belenchia, E. Castro-Ruiz, C. Budroni, M. Zych, v. C. Brukner, and R. B. Mann, (2020), arXiv:2002.06208 [quant-ph].
- [72] M. Horodecki, P. Horodecki, and R. Horodecki, Phys. Rev. Lett. **84**, 4260 (2000).
- [73] N. Klco and M. J. Savage, Phys. Rev. A **102**, 012619 (2020), arXiv:1912.03577 [quant-ph].
- [74] T. Yu and J. H. Eberly, Phys. Rev. Lett. **93**, 140404 (2004).
- [75] P. J. Dodd and J. J. Halliwell, Physical Review A **69** (2004), 10.1103/physreva.69.052105.
- [76] M. P. Almeida, F. de Melo, M. Hor-Meyll, A. Salles, S. P. Walborn, P. H. S. Ribeiro, and L. Davidovich, Science **316**, 579 (2007), <https://science.sciencemag.org/content/316/5824/579.full.pdf>.
- [77] T. Yu and J. H. Eberly, Science **323**, 598 (2009), <https://science.sciencemag.org/content/323/5914/598.full.pdf>.
- [78] Z. Davoudi and M. J. Savage, Phys. Rev. D **86**, 054505 (2012), arXiv:1204.4146 [hep-lat].
- [79] K. Symanzik, Nuclear Physics B **226**, 187 (1983).
- [80] T. Luu and M. J. Savage, Phys. Rev. D **83**, 114508 (2011), arXiv:1101.3347 [hep-lat].
- [81] G. Adesso, A. Serafini, and F. Illuminati, Phys. Rev. A **70**, 022318 (2004).
- [82] M. M. Wolf, G. Giedke, and J. I. Cirac, Phys. Rev. Lett. **96**, 080502 (2006).
- [83] H. Muller, S. Koonin, R. Seki, and U. van Kolck, Phys. Rev. C **61**, 044320 (2000), arXiv:nucl-th/9910038.
- [84] T. A. Lahde and U.-G. Meissner, *Nuclear Lattice Effective Field Theory: An introduction*, Vol. 957 (Springer, 2019).
- [85] D. Lee, Front. in Phys. **8**, 174 (2020).
- [86] D. Lee, Prog. Part. Nucl. Phys. **63**, 117 (2009), arXiv:0804.3501 [nucl-th].
- [87] G. 't Hooft, Nucl. Phys. **B72**, 461 (1974), [,337(1973)].
- [88] E. Witten, Annals Phys. **128**, 363 (1980).
- [89] R. F. Dashen, E. E. Jenkins, and A. V. Manohar, Phys. Rev. D **49**, 4713 (1994), [Erratum: Phys.Rev.D 51, 2489 (1995)], arXiv:hep-ph/9310379.
- [90] R. F. Dashen, E. E. Jenkins, and A. V. Manohar, Phys. Rev. D **51**, 3697 (1995), arXiv:hep-ph/9411234.
- [91] D. B. Kaplan and M. J. Savage, Phys. Lett. B **365**, 244 (1996), arXiv:hep-ph/9509371.
- [92] D. B. Kaplan and A. V. Manohar, Phys. Rev. C **56**, 76 (1997), arXiv:nucl-th/9612021.
- [93] V. Coffman, J. Kundu, and W. K. Wootters, Phys. Rev. A **61**, 052306 (2000), arXiv:quant-ph/9907047.
- [94] W. Dur, G. Vidal, and J. Cirac, Phys. Rev. A **62**, 062314 (2000), arXiv:quant-ph/0005115.
- [95] R. Lohmayer, A. Osterloh, J. Siewert, and A. Uhlmann, Phys. Rev. Lett. **97**, 260502 (2006).
- [96] M. Rangamani and M. Rota, J. Phys. A **48**, 385301 (2015), arXiv:1505.03696 [hep-th].
- [97] M. Lüscher, Commun.Math.Phys. **105**, 153 (1986).
- [98] M. Lüscher, Nucl.Phys **B354**, 531 (1991).

- [99] M. Lüscher and U. Wolff, Nucl. Phys. **B339**, 222 (1990).
- [100] E. E. Jenkins and A. V. Manohar, Phys. Lett. B **255**, 558 (1991).
- [101] S. Beane, P. F. Bedaque, M. Savage, and U. van Kolck, Nucl. Phys. A **700**, 377 (2002), arXiv:nucl-th/0104030.
- [102] M. C. Birse, Phys. Rev. C **74**, 014003 (2006).
- [103] D. B. Kaplan, (2019), arXiv:1905.07485 [nucl-th].
- [104] R. D. Young, D. B. Leinweber, and A. W. Thomas, Nucl. Phys. B Proc. Suppl. **141**, 233 (2005).
- [105] S. R. White, Phys. Rev. Lett. **69**, 2863 (1992).
- [106] G. Vidal, Phys. Rev. Lett. **91**, 147902 (2003).
- [107] U. Schollwöck, Rev. Mod. Phys. **77**, 259 (2005).
- [108] F. Verstraete, V. Murg, and J. I. Cirac, Advances in Physics **57**, 143 (2008), arXiv:0907.2796 [quant-ph].
- [109] Wolfram Research, Inc., “Mathematica, Version 11.1,” Champaign, IL, 2020.
- [110] Advanpix LLC., “Multiprecision computing toolbox for matlab,” .
- [111] MATLAB, *version 9.8.0.1396136 (R2020a) Update 3* (The MathWorks Inc., Natick, Massachusetts, 2020).

Appendix A: Figure Tables

x	y	$\psi_0(x, y)$	10	4	-0.029216	2	8	-0.041270	32	0	-0.0053146	37	4	-0.0067524	29	8	-0.055241
6	0	0.0053146	11	4	-0.0054380	3	8	-0.030045	29	1	-0.0044180	27	5	-0.0027471	30	8	-0.10603
3	1	0.0060582	1	5	0.0068186	4	8	0.0076432	30	1	-0.0042535	28	5	-0.023216	31	8	-0.11486
4	1	0.0068117	2	5	-0.038103	5	8	0.053102	31	1	-0.0072781	29	5	-0.11490	32	8	-0.092581
5	1	0.010010	3	5	-0.014644	6	8	0.092581	32	1	0.077618	30	5	-0.16310	33	8	-0.053102
6	1	-0.077618	4	5	0.034162	7	8	0.11486	33	1	-0.010010	31	5	-0.16628	34	8	-0.0076432
7	1	0.0072781	5	5	0.089135	8	8	0.10603	34	1	-0.0068117	32	5	-0.13717	35	8	0.030045
8	1	0.0042535	6	5	0.13717	9	8	0.055241	35	1	-0.0060582	33	5	-0.089135	36	8	0.041270
9	1	0.0044180	7	5	0.16628	10	8	-0.029216	28	2	-0.013301	34	5	-0.034162	37	8	-0.0067524
2	2	0.0082886	8	5	0.16310	11	8	-0.0054380	29	2	0.089283	35	5	0.014644	27	9	-0.0012799
3	2	-0.043739	9	5	0.11490	1	9	0.0057025	30	2	0.052302	36	5	0.038103	28	9	0.089620
4	2	-0.050578	10	5	0.023216	2	9	-0.034449	31	2	0.031974	37	5	-0.0068186	29	9	0.028781
5	2	-0.040683	11	5	0.0027471	3	9	-0.046326	32	2	0.043948	26	6	0.0037411	30	9	-0.022905
6	2	-0.043948	0	6	0.0049114	4	9	-0.027783	33	2	0.040683	27	6	0.10248	31	9	-0.039338
7	2	-0.031974	1	6	-0.036499	5	9	0.0019202	34	2	0.050578	28	6	-0.029073	32	9	-0.026263
8	2	-0.052302	2	6	-0.043229	6	9	0.026263	35	2	0.043739	29	6	-0.13402	33	9	-0.0019202
9	2	-0.089283	3	6	-0.0099229	7	9	0.039338	36	2	-0.0082886	30	6	-0.18274	34	9	0.027783
10	2	0.013301	4	6	0.043510	8	9	0.022905	27	3	-0.0012799	31	6	-0.18416	35	9	0.046326
1	3	0.0057025	5	6	0.10181	9	9	-0.028781	28	3	0.089620	32	6	-0.15268	36	9	0.034449
2	3	-0.034449	6	6	0.15268	10	9	-0.089620	29	3	0.028781	33	6	-0.10181	37	9	-0.0057025
3	3	-0.046326	7	6	0.18416	11	9	0.0012799	30	3	-0.022905	34	6	-0.043510	28	10	-0.013301
4	3	-0.027783	8	6	0.18274	2	10	0.0082886	31	3	-0.039338	35	6	0.0099229	29	10	0.089283
5	3	0.0019202	9	6	0.13402	3	10	-0.043739	32	3	-0.026263	36	6	0.043229	30	10	0.052302
6	3	0.026263	10	6	0.029073	4	10	-0.050578	33	3	-0.0019202	37	6	0.036499	31	10	0.031974
7	3	0.039338	11	6	-0.10248	5	10	-0.040683	34	3	0.027783	38	6	-0.0049114	32	10	0.043948
8	3	0.022905	12	6	-0.0037411	6	10	-0.043948	35	3	0.046326	27	7	-0.0027471	33	10	0.040683
9	3	-0.028781	1	7	0.0068186	7	10	-0.031974	36	3	0.034449	28	7	-0.023216	34	10	0.050578
10	3	-0.089620	2	7	-0.038103	8	10	-0.052302	37	3	-0.0057025	29	7	-0.11490	35	10	0.043739
11	3	0.0012799	3	7	-0.014644	9	10	-0.089283	27	4	0.0054380	30	7	-0.16310	36	10	-0.0082886
1	4	0.0067524	4	7	0.034162	10	10	0.013301	28	4	0.029216	31	7	-0.16628	29	11	-0.0044180
2	4	-0.041270	5	7	0.089135	3	11	0.0060582	29	4	-0.055241	32	7	-0.13717	30	11	-0.0042535
3	4	-0.030045	6	7	0.13717	4	11	0.0068117	30	4	-0.10603	33	7	-0.089135	31	11	-0.0072781
4	4	0.0076432	7	7	0.16628	5	11	0.010010	31	4	-0.11486	34	7	-0.034162	32	11	0.077618
5	4	0.053102	8	7	0.16310	6	11	-0.077618	32	4	-0.092581	35	7	0.014644	33	11	-0.010010
6	4	0.092581	9	7	0.11490	7	11	0.0072781	33	4	-0.053102	36	7	0.038103	34	11	-0.0068117
7	4	0.11486	10	7	0.023216	8	11	0.0042535	34	4	-0.0076432	37	7	-0.0068186	35	11	-0.0060582
8	4	0.10603	11	7	0.0027471	9	11	0.0044180	35	4	0.030045	27	8	0.0054380	32	12	-0.0053146
9	4	0.055241	1	8	0.0067524	6	12	0.0053146	36	4	0.041270	28	8	0.029216			

TABLE I. Wavefunction amplitudes shown in the left panel of Fig. 2.

x	y	$\psi_0(x, y)$	11	3	-3.1143×10^{-9}	5	6	0.24398	11	8	-5.7750×10^{-8}
6	0	4.9034×10^{-8}	1	4	-8.2163×10^{-8}	6	6	-0.37969	1	9	-5.3318×10^{-9}
3	1	-5.2388×10^{-9}	2	4	-8.0923×10^{-6}	7	6	0.23827	2	9	-2.7117×10^{-7}
4	1	-8.1054×10^{-8}	3	4	0.00061368	8	6	-0.066852	3	9	-0.000013289
5	1	-1.3491×10^{-6}	4	4	-0.0083757	9	6	0.0086482	4	9	0.00061389
6	1	6.5912×10^{-6}	5	4	0.039844	10	6	-0.00045085	5	9	-0.0045493
7	1	-1.3237×10^{-6}	6	4	-0.069559	11	6	4.0623×10^{-6}	6	9	0.0092643
8	1	-6.7897×10^{-8}	7	4	0.039077	12	6	6.6846×10^{-8}	7	9	-0.0044675
9	1	-3.8544×10^{-9}	8	4	-0.0081646	1	7	-1.3578×10^{-6}	8	9	0.00061098
2	2	-8.6614×10^{-9}	9	4	0.00060715	2	7	0.00019088	9	9	-0.000015291
3	2	-2.7111×10^{-7}	10	4	-9.2898×10^{-6}	3	7	-0.0045545	10	9	-2.5654×10^{-7}
4	2	-8.1358×10^{-6}	11	4	-5.7750×10^{-8}	4	7	0.039877	11	9	-3.1143×10^{-9}
5	2	0.00019040	1	5	-1.3578×10^{-6}	5	7	-0.15121	2	10	-8.6614×10^{-9}
6	2	-0.00051386	2	5	0.00019088	6	7	0.24273	3	10	-2.7111×10^{-7}
7	2	0.00018701	3	5	-0.0045545	7	7	-0.14799	4	10	-8.1358×10^{-6}
8	2	-8.9529×10^{-6}	4	5	0.039877	8	7	0.038412	5	10	0.00019040
9	2	-2.5605×10^{-7}	5	5	-0.15121	9	7	-0.0043252	6	10	-0.00051386
10	2	-5.1844×10^{-9}	6	5	0.24273	10	7	0.00017830	7	10	0.00018701
1	3	-5.3318×10^{-9}	7	5	-0.14799	11	7	-1.2394×10^{-6}	8	10	-8.9529×10^{-6}
2	3	-2.7117×10^{-7}	8	5	0.038412	1	8	-8.2163×10^{-8}	9	10	-2.5605×10^{-7}
3	3	-0.000013289	9	5	-0.0043252	2	8	-8.0923×10^{-6}	10	10	-5.1844×10^{-9}
4	3	0.00061389	10	5	0.00017830	3	8	0.00061368	3	11	-5.2388×10^{-9}
5	3	-0.0045493	11	5	-1.2394×10^{-6}	4	8	-0.0083757	4	11	-8.1054×10^{-8}
6	3	0.0092643	0	6	4.4273×10^{-8}	5	8	0.039844	5	11	-1.3491×10^{-6}
7	3	-0.0044675	1	6	7.0459×10^{-6}	6	8	-0.069559	6	11	6.5912×10^{-6}
8	3	0.00061098	2	6	-0.00052161	7	8	0.039077	7	11	-1.3237×10^{-6}
9	3	-0.000015291	3	6	0.0093308	8	8	-0.0081646	8	11	-6.7897×10^{-8}
10	3	-2.5654×10^{-7}	4	6	-0.069963	9	8	0.00060715	9	11	-3.8544×10^{-9}
						10	8	-9.2898×10^{-6}	6	12	4.9034×10^{-8}

TABLE II. Wavefunction amplitudes shown in the right panel of Fig. 2.

$d_{lat} = 9$					
\tilde{r}/d_{avg}	\mathcal{N}				
0.553	1.47×10^{-3}				
0.691	7.57×10^{-4}				
0.829	3.46×10^{-4}	$d_{lat} = 11$		3.06	2.91×10^{-9}
0.968	1.34×10^{-4}	0.106	2.35×10^{-2}	3.28	9.19×10^{-10}
1.11	5.16×10^{-5}	0.211	9.16×10^{-3}	3.38	4.81×10^{-10}
		0.317	5.47×10^{-3}	3.49	2.35×10^{-10}
$d_{lat} = 7$					
\tilde{r}/d_{avg}	\mathcal{N}				
0.553	1.20×10^{-3}	1.52	8.13×10^{-6}		
0.737	5.90×10^{-4}	1.66	4.78×10^{-6}	0.634	1.27×10^{-3}
0.922	2.58×10^{-4}	1.8	2.67×10^{-6}	0.74	7.16×10^{-4}
1.11	9.09×10^{-5}	1.94	1.36×10^{-6}	0.845	3.69×10^{-4}
1.29	2.29×10^{-5}	2.07	6.15×10^{-7}	0.951	1.78×10^{-4}
1.47	6.81×10^{-6}	2.21	2.25×10^{-7}	1.06	8.98×10^{-5}
1.66	2.91×10^{-6}	2.35	6.57×10^{-8}	1.16	5.09×10^{-5}
1.84	1.32×10^{-6}	2.49	2.40×10^{-8}	1.27	3.14×10^{-5}
2.03	5.12×10^{-7}	2.63	1.18×10^{-8}	1.37	2.03×10^{-5}
2.21	1.57×10^{-7}	2.76	6.68×10^{-9}	1.48	1.32×10^{-5}
2.4	4.84×10^{-8}	2.9	4.01×10^{-9}	1.58	8.46×10^{-6}
2.58	1.29×10^{-8}	3.04	2.39×10^{-9}	1.69	5.21×10^{-6}
2.77	2.41×10^{-9}	3.18	1.33×10^{-9}	1.8	3.02×10^{-6}
2.95	7.82×10^{-10}	3.32	6.03×10^{-10}	1.9	1.61×10^{-6}
3.13	3.66×10^{-10}	3.46	1.80×10^{-10}	2.01	7.76×10^{-7}
3.32	1.83×10^{-10}	3.59	5.06×10^{-11}	2.11	3.41×10^{-7}
3.5	8.01×10^{-11}	3.73	1.69×10^{-11}	2.22	1.48×10^{-7}
3.69	1.32×10^{-11}	3.87	4.61×10^{-12}	2.32	7.27×10^{-8}
		4.01	1.13×10^{-12}	2.43	4.12×10^{-8}
		4.15	4.72×10^{-13}	2.54	2.57×10^{-8}
		4.29	2.56×10^{-13}	2.64	1.68×10^{-8}
		4.42	1.52×10^{-13}	2.75	1.12×10^{-8}
		4.56	9.09×10^{-14}	2.85	7.43×10^{-9}
		4.7	5.05×10^{-14}	2.96	4.77×10^{-9}
		4.84	2.17×10^{-14}		
		4.98	1.39×10^{-16}		

TABLE III. Logarithmic negativity as a function of separation measured in units of the averaged region diameter with an N-type boundary appearing in the left panel of Fig. 3.

$d_{lat} = 13$		$d_{lat} = 15$	
\tilde{r}/d_{avg}	\mathcal{N}	\tilde{r}/d_{avg}	\mathcal{N}
0.0885	2.90×10^{-2}	3.72	8.43×10^{-11}
0.177	1.27×10^{-2}	3.81	5.45×10^{-11}
0.266	7.93×10^{-3}	3.89	3.45×10^{-11}
0.354	5.17×10^{-3}	3.98	2.15×10^{-11}
0.443	3.40×10^{-3}	4.07	1.32×10^{-11}
0.531	2.20×10^{-3}	4.16	7.89×10^{-12}
0.62	1.37×10^{-3}	4.25	4.55×10^{-12}
0.708	8.06×10^{-4}	4.34	2.52×10^{-12}
0.797	4.46×10^{-4}	4.43	1.36×10^{-12}
0.885	2.42×10^{-4}	4.51	7.28×10^{-13}
0.974	1.38×10^{-4}	4.69	1.85×10^{-13}
1.06	8.51×10^{-5}	4.78	9.15×10^{-14}
1.15	5.54×10^{-5}	4.87	5.04×10^{-14}
1.24	3.73×10^{-5}	4.96	3.11×10^{-14}
1.33	2.53×10^{-5}	5.05	2.08×10^{-14}
1.42	1.71×10^{-5}	5.13	1.45×10^{-14}
1.5	1.13×10^{-5}	5.22	1.04×10^{-14}
1.59	7.27×10^{-6}	5.31	7.45×10^{-15}
1.68	4.46×10^{-6}	5.4	5.30×10^{-15}
1.77	2.62×10^{-6}	5.49	3.67×10^{-15}
1.86	1.49×10^{-6}	5.58	2.41×10^{-15}
1.95	8.45×10^{-7}	5.67	1.46×10^{-15}
2.04	4.90×10^{-7}	5.75	7.89×10^{-16}
2.12	2.96×10^{-7}	5.84	3.85×10^{-16}
2.21	1.88×10^{-7}	5.93	1.71×10^{-16}
2.3	1.24×10^{-7}	6.02	6.10×10^{-17}
2.39	8.46×10^{-8}	6.11	1.64×10^{-17}
2.48	5.85×10^{-8}	6.2	6.17×10^{-18}
2.57	4.06×10^{-8}	6.28	3.19×10^{-18}
2.66	2.79×10^{-8}	6.37	1.87×10^{-18}
2.74	1.88×10^{-8}	6.46	1.13×10^{-18}
2.83	1.23×10^{-8}	6.55	6.74×10^{-19}
2.92	7.80×10^{-9}	6.64	3.68×10^{-19}
3.01	4.72×10^{-9}	6.73	1.70×10^{-19}
3.1	2.73×10^{-9}	6.82	7.10×10^{-20}
3.19	1.52×10^{-9}	6.9	3.36×10^{-20}
3.28	8.48×10^{-10}	6.99	1.81×10^{-20}
3.36	4.96×10^{-10}	7.08	1.02×10^{-20}
3.45	3.07×10^{-10}	7.17	5.45×10^{-21}
3.54	1.97×10^{-10}	7.26	2.35×10^{-21}
3.63	1.29×10^{-10}	7.35	1.61×10^{-22}

\tilde{r}/d_{avg}	\mathcal{N}	\tilde{r}/d_{avg}	\mathcal{N}
2.91	6.19×10^{-9}	2.98	3.75×10^{-9}
3.06	2.32×10^{-9}	3.14	1.50×10^{-9}
3.29	6.99×10^{-10}	3.37	4.91×10^{-10}
3.44	3.47×10^{-10}	3.52	2.43×10^{-10}
3.6	1.68×10^{-10}	3.6	6.43×10^{-18}
3.67	1.14×10^{-10}	3.75	7.67×10^{-11}
3.75	6.5×10^{-18}	3.83	5.10×10^{-11}
3.98	6.99×10^{-18}	4.05	4.43×10^{-11}
4.15	5.96×10^{-19}	4.21	5.65×10^{-12}
4.21	3.28×10^{-19}	4.28	3.47×10^{-12}
4.36	8.57×10^{-20}	4.36	2.15×10^{-12}
4.44	3.49×10^{-20}	4.44	1.39×10^{-12}
4.51	1.28×10^{-20}	4.51	9.32×10^{-13}
4.59	6.08×10^{-21}	4.59	6.51×10^{-13}
4.67	3.60×10^{-21}	4.67	4.67×10^{-13}
4.74	2.39×10^{-21}	4.74	7.5×10^{-13}
4.82	1.68×10^{-21}	4.82	3.40×10^{-13}
4.91	1.68×10^{-21}	4.91	7.57×10^{-13}
4.99	1.22×10^{-21}	4.99	7.65×10^{-13}
5.05	1.22×10^{-21}	5.05	5.65×10^{-12}
5.13	1.22×10^{-21}	5.13	7.04×10^{-12}
5.22	1.22×10^{-21}	5.22	7.12×10^{-12}
5.31	1.22×10^{-21}	5.31	1.75×10^{-19}
5.4	1.22×10^{-21}	5.4	9.09×10^{-12}
5.49	1.22×10^{-21}	5.49	6.96×10^{-19}
5.58	1.22×10^{-21}	5.58	3.28×10^{-19}
5.67	1.22×10^{-21}	5.67	7.04×10^{-19}
5.75	1.22×10^{-21}	5.75	8.57×10^{-20}
5.84	1.22×10^{-21}	5.84	3.49×10^{-20}
5.93	1.22×10^{-21}	5.93	1.28×10^{-20}
6.02	1.22×10^{-21}	6.02	6.08×10^{-21}
6.11	1.22×10^{-21}	6.11	3.60×10^{-21}
6.2	1.22×10^{-21}	6.2	2.39×10^{-21}
6.28	1.22×10^{-21}	6.28	1.68×10^{-21}
6.46	1.22×10^{-21}	6.46	1.68×10^{-21}
6.55	1.22×10^{-21}	6.55	1.22×10^{-21}
6.64	1.22×10^{-21}	6.64	8.03×10^{-22}
6.73	1.22×10^{-21}	6.73	8.96×10^{-22}
6.82	1.22×10^{-21}	6.82	6.57×10^{-22}
6.9	1.22×10^{-21}	6.9	4.74×10^{-22}
6.99	1.22×10^{-21}	6.99	2.13×10^{-22}
7.08	1.22×10^{-21}	7.08	3.29×10^{-22}
7.17	1.22×10^{-21}	7.17	8.04×10^{-24}
7.26	1.22×10^{-21}	7.26	4.37×10^{-23}
7.35	1.22×10^{-21}	7.35	2.08×10^{-24}
7.44	1.22×10^{-21}	7.44	4.51×10^{-25}

TABLE IV. Logarithmic negativity as a function of separation measured in units of the averaged region diameter with an N-type boundary appearing in the left panel of Fig. 3.

$d_{lat} = 17$							
\tilde{r}/d_{avg}	\mathcal{N}	2.45	8.51×10^{-8}	4.89	1.68×10^{-13}	7.34	4.37×10^{-20}
0.0661	3.98×10^{-2}	2.51	6.00×10^{-8}	4.96	1.24×10^{-13}	7.4	2.60×10^{-20}
0.132	2.01×10^{-2}	2.58	4.13×10^{-8}	5.02	8.98×10^{-14}	7.47	1.61×10^{-20}
0.198	1.34×10^{-2}	2.64	2.77×10^{-8}	5.09	6.33×10^{-14}	7.53	1.04×10^{-20}
0.264	9.33×10^{-3}	2.71	1.80×10^{-8}	5.16	4.37×10^{-14}	7.6	7.05×10^{-21}
0.33	6.60×10^{-3}	2.78	1.14×10^{-8}	5.22	2.94×10^{-14}	7.67	4.88×10^{-21}
0.397	4.68×10^{-3}	2.84	7.09×10^{-9}	5.29	1.94×10^{-14}	7.73	3.41×10^{-21}
0.463	3.29×10^{-3}	2.91	4.46×10^{-9}	5.35	1.25×10^{-14}	7.8	2.39×10^{-21}
0.529	2.26×10^{-3}	2.97	2.92×10^{-9}	5.42	7.81×10^{-15}	7.86	1.65×10^{-21}
0.595	1.50×10^{-3}	3.04	2.00×10^{-9}	5.49	4.77×10^{-15}	7.93	1.12×10^{-21}
0.661	9.66×10^{-4}	3.11	1.43×10^{-9}	5.55	2.92×10^{-15}	8.	7.44×10^{-22}
0.727	6.07×10^{-4}	3.17	1.06×10^{-9}	5.62	1.86×10^{-15}	8.06	4.79×10^{-22}
0.793	3.85×10^{-4}	3.24	7.97×10^{-10}	5.68	1.24×10^{-15}	8.13	3.00×10^{-22}
0.859	2.53×10^{-4}	3.3	6.07×10^{-10}	5.75	8.70×10^{-16}	8.2	1.84×10^{-22}
0.925	1.74×10^{-4}	3.37	4.65×10^{-10}	5.82	6.31×10^{-16}	8.26	1.08×10^{-22}
0.991	1.24×10^{-4}	3.44	3.55×10^{-10}	5.88	4.68×10^{-16}	8.33	5.97×10^{-23}
1.06	9.10×10^{-5}	3.5	2.69×10^{-10}	5.95	3.51×10^{-16}	8.39	2.91×10^{-23}
1.12	6.73×10^{-5}	3.57	2.01×10^{-10}	6.01	2.65×10^{-16}	8.46	1.25×10^{-23}
1.19	5.00×10^{-5}	3.63	1.47×10^{-10}	6.08	1.99×10^{-16}	8.53	5.85×10^{-24}
1.26	3.70×10^{-5}	3.7	1.05×10^{-10}	6.15	1.47×10^{-16}	8.59	3.31×10^{-24}
1.32	2.70×10^{-5}	3.77	7.28×10^{-11}	6.21	1.07×10^{-16}	8.66	2.14×10^{-24}
1.39	1.94×10^{-5}	3.83	4.92×10^{-11}	6.28	7.54×10^{-17}	8.72	1.49×10^{-24}
1.45	1.37×10^{-5}	3.9	3.25×10^{-11}	6.34	5.12×10^{-17}	8.79	1.08×10^{-24}
1.52	9.36×10^{-6}	3.97	2.10×10^{-11}	6.41	3.35×10^{-17}	8.86	7.99×10^{-25}
1.59	6.24×10^{-6}	4.03	1.35×10^{-11}	6.48	2.13×10^{-17}	8.92	5.96×10^{-25}
1.65	4.09×10^{-6}	4.1	8.66×10^{-12}	6.54	1.34×10^{-17}	8.99	4.44×10^{-25}
1.72	2.69×10^{-6}	4.16	5.61×10^{-12}	6.61	8.39×10^{-18}	9.05	3.25×10^{-25}
1.78	1.81×10^{-6}	4.23	3.70×10^{-12}	6.68	5.28×10^{-18}	9.12	2.30×10^{-25}
1.85	1.26×10^{-6}	4.3	2.50×10^{-12}	6.74	3.32×10^{-18}	9.19	1.54×10^{-25}
1.92	9.04×10^{-7}	4.36	1.73×10^{-12}	6.81	2.08×10^{-18}	9.25	9.20×10^{-26}
1.98	6.66×10^{-7}	4.43	1.24×10^{-12}	6.87	1.30×10^{-18}	9.32	4.39×10^{-26}
2.05	4.98×10^{-7}	4.49	9.05×10^{-13}	6.94	8.19×10^{-19}	9.38	1.04×10^{-26}
2.11	3.76×10^{-7}	4.56	6.75×10^{-13}	7.01	5.17×10^{-19}	9.45	1.06×10^{-27}
2.18	2.85×10^{-7}	4.63	5.10×10^{-13}	7.07	3.26×10^{-19}	9.52	3.19×10^{-28}
2.25	2.15×10^{-7}	4.69	3.89×10^{-13}	7.14	2.04×10^{-19}	9.58	1.11×10^{-28}
2.31	1.60×10^{-7}	4.76	2.96×10^{-13}	7.2	1.25×10^{-19}	9.65	1.39×10^{-29}
2.38	1.18×10^{-7}	4.82	2.24×10^{-13}	7.27	7.43×10^{-20}		

TABLE V. Logarithmic negativity as a function of separation measured in units of the averaged region diameter with an N-type boundary appearing in the left panel of Fig. 3.

$d_{lat} = 19$									
\tilde{r}/d_{avg}	\mathcal{N}	1.8	1.81×10^{-6}	3.6	1.96×10^{-10}	5.4	1.02×10^{-14}	7.2	3.41×10^{-19}
0.058	4.98×10^{-2}	1.86	1.35×10^{-6}	3.66	1.41×10^{-10}	5.46	7.53×10^{-15}	7.26	2.54×10^{-19}
0.116	2.61×10^{-2}	1.92	1.02×10^{-6}	3.71	9.99×10^{-11}	5.51	5.67×10^{-15}	7.31	1.91×10^{-19}
0.174	1.75×10^{-2}	1.97	7.76×10^{-7}	3.77	6.99×10^{-11}	5.57	4.32×10^{-15}	7.37	1.46×10^{-19}
0.232	1.24×10^{-2}	2.03	5.95×10^{-7}	3.83	4.85×10^{-11}	5.63	3.32×10^{-15}	7.43	1.11×10^{-19}
0.29	8.94×10^{-3}	2.09	4.57×10^{-7}	3.89	3.37×10^{-11}	5.69	2.56×10^{-15}	7.49	8.53×10^{-20}
0.348	6.52×10^{-3}	2.15	3.50×10^{-7}	3.95	2.37×10^{-11}	5.75	1.97×10^{-15}	7.55	6.50×10^{-20}
0.406	4.75×10^{-3}	2.21	2.67×10^{-7}	4.01	1.69×10^{-11}	5.8	1.52×10^{-15}	7.6	4.91×10^{-20}
0.464	3.43×10^{-3}	2.26	2.02×10^{-7}	4.06	1.23×10^{-11}	5.86	1.16×10^{-15}	7.66	3.66×10^{-20}
0.522	2.43×10^{-3}	2.32	1.51×10^{-7}	4.12	9.14×10^{-12}	5.92	8.77×10^{-16}	7.72	2.67×10^{-20}
0.58	1.69×10^{-3}	2.38	1.12×10^{-7}	4.18	6.88×10^{-12}	5.98	6.57×10^{-16}	7.78	1.89×10^{-20}
0.638	1.15×10^{-3}	2.44	8.15×10^{-8}	4.24	5.23×10^{-12}	6.04	4.86×10^{-16}	7.84	1.30×10^{-20}
0.697	7.75×10^{-4}	2.5	5.84×10^{-8}	4.3	3.99×10^{-12}	6.09	3.56×10^{-16}	7.89	8.61×10^{-21}
0.755	5.28×10^{-4}	2.55	4.13×10^{-8}	4.35	3.05×10^{-12}	6.15	2.58×10^{-16}	7.95	5.52×10^{-21}
0.813	3.69×10^{-4}	2.61	2.89×10^{-8}	4.41	2.31×10^{-12}	6.21	1.85×10^{-16}	8.01	3.44×10^{-21}
0.871	2.64×10^{-4}	2.67	2.02×10^{-8}	4.47	1.74×10^{-12}	6.27	1.32×10^{-16}	8.07	2.10×10^{-21}
0.929	1.94×10^{-4}	2.73	1.42×10^{-8}	4.53	1.30×10^{-12}	6.33	9.31×10^{-17}	8.13	1.27×10^{-21}
0.987	1.45×10^{-4}	2.79	1.02×10^{-8}	4.59	9.59×10^{-13}	6.38	6.51×10^{-17}	8.18	7.92×10^{-22}
1.04	1.10×10^{-4}	2.9	5.54×10^{-9}	4.7	5.12×10^{-13}	6.5	3.08×10^{-17}	8.3	3.53×10^{-22}
1.1	8.36×10^{-5}	2.96	4.18×10^{-9}	4.76	3.73×10^{-13}	6.56	2.08×10^{-17}	8.36	2.50×10^{-22}
1.16	6.36×10^{-5}	3.02	3.19×10^{-9}	4.82	2.73×10^{-13}	6.62	1.40×10^{-17}	8.42	1.81×10^{-22}
1.22	4.82×10^{-5}	3.08	2.45×10^{-9}	4.88	1.99×10^{-13}	6.68	9.37×10^{-18}	8.47	1.33×10^{-22}
1.28	3.61×10^{-5}	3.13	1.89×10^{-9}	4.93	1.46×10^{-13}	6.73	6.28×10^{-18}	8.53	9.83×10^{-23}
1.34	2.68×10^{-5}	3.19	1.46×10^{-9}	4.99	1.06×10^{-13}	6.79	4.23×10^{-18}	8.59	7.24×10^{-23}
1.39	1.95×10^{-5}	3.25	1.12×10^{-9}	5.05	7.65×10^{-14}	6.85	2.85×10^{-18}	8.65	5.28×10^{-23}
1.45	1.40×10^{-5}	3.31	8.56×10^{-10}	5.11	5.46×10^{-14}	6.91	1.94×10^{-18}	8.71	3.79×10^{-23}
1.51	9.92×10^{-6}	3.37	6.51×10^{-10}	5.17	3.87×10^{-14}	6.97	1.32×10^{-18}	8.76	2.65×10^{-23}
1.57	6.94×10^{-6}	3.42	4.90×10^{-10}	5.22	2.74×10^{-14}	7.02	9.18×10^{-19}	8.82	1.80×10^{-23}
1.63	4.86×10^{-6}	3.48	3.66×10^{-10}	5.28	1.94×10^{-14}	7.08	6.47×10^{-19}	8.88	1.17×10^{-23}
1.68	3.43×10^{-6}	3.54	2.70×10^{-10}	5.34	1.39×10^{-14}	7.14	4.65×10^{-19}	8.94	7.27×10^{-24}
1.74	2.47×10^{-6}								

TABLE VI. Logarithmic negativity as a function of separation measured in units of the averaged region diameter with an N-type boundary appearing in the left panel of Fig. 3.

$d_{lat} = 21$				$d_{lat} = 23$				$d_{lat} = 25$				$d_{lat} = 27$				$d_{lat} = 29$	
\tilde{r}/d_{avg}		\mathcal{N}		\tilde{r}/d_{avg}													
2.68	1.72×10^{-8}	2.69	1.58×10^{-8}	2.96	4.59×10^{-9}	2.7	1.53×10^{-8}	2.66	2.07×10^{-8}	2.89	6.73×10^{-9}	2.65	2.30×10^{-8}	2.87	8.13×10^{-9}	2.53	2.53×10^{-9}
2.99	3.64×10^{-9}	3.26	1.12×10^{-9}	3.22	1.20×10^{-9}	3.48	2.61×10^{-10}	3.37	5.11×10^{-10}	3.13	1.98×10^{-9}	3.61	1.39×10^{-10}	3.53	2.14×10^{-10}	3.31	6.95×10^{-10}
3.3	8.75×10^{-10}	3.54	2.21×10^{-10}	3.74	6.64×10^{-11}	4.01	1.96×10^{-11}	3.85	4.44×10^{-11}	4.27	5.25×10^{-12}	4.08	1.39×10^{-11}	3.97	2.55×10^{-11}	3.75	7.51×10^{-11}
3.61	1.52×10^{-10}	3.82	4.56×10^{-11}	4.01	1.96×10^{-11}	3.74	6.64×10^{-11}	4.01	1.96×10^{-11}	4.27	5.25×10^{-12}	4.32	3.81×10^{-12}	4.19	7.75×10^{-12}	4.41	2.2×10^{-12}
3.92	2.60×10^{-11}	4.11	1.18×10^{-11}	4.27	5.25×10^{-12}	4.53	1.19×10^{-12}	4.56	9.90×10^{-13}	4.32	3.81×10^{-12}	4.08	1.39×10^{-11}	4.63	6.91×10^{-13}	4.41	2.2×10^{-12}
4.23	6.18×10^{-12}	4.39	2.77×10^{-12}	4.53	1.19×10^{-12}	4.79	2.65×10^{-13}	4.56	9.90×10^{-13}	4.79	2.65×10^{-13}	5.05	7.62×10^{-14}	4.85	2.92×10^{-13}	5.07	7.55×10^{-14}
4.54	1.33×10^{-12}	4.67	5.72×10^{-13}	4.79	2.65×10^{-13}	5.05	7.62×10^{-14}	5.04	9.12×10^{-14}	5.31	2.18×10^{-14}	5.27	2.64×10^{-14}	5.29	2.27×10^{-14}	5.51	6.62×10^{-15}
4.85	2.17×10^{-13}	4.96	1.12×10^{-13}	5.05	7.62×10^{-14}	5.31	2.18×10^{-14}	5.27	2.64×10^{-14}	5.57	5.10×10^{-15}	5.51	7.18×10^{-15}	5.74	$2. \times 10^{-15}$	5.51	6.62×10^{-15}
5.16	3.24×10^{-14}	5.24	2.91×10^{-14}	5.31	2.18×10^{-14}	5.84	1.15×10^{-15}	5.75	1.89×10^{-15}	5.84	1.15×10^{-15}	6.1	2.63×10^{-16}	5.99	5.22×10^{-16}	5.96	6.81×10^{-16}
5.47	6.89×10^{-15}	5.52	7.52×10^{-15}	5.57	5.10×10^{-15}	5.57	5.10×10^{-15}	5.51	7.18×10^{-15}	5.57	5.10×10^{-15}	6.23	1.51×10^{-16}	6.18	2.29×10^{-16}	6.62	1.99×10^{-17}
5.78	1.50×10^{-15}	5.81	1.44×10^{-15}	5.84	1.15×10^{-15}	6.22	1.89×10^{-17}	6.46	3.98×10^{-17}	6.22	1.89×10^{-17}	6.46	3.98×10^{-17}	6.4	6.81×10^{-17}	6.62	1.99×10^{-17}
6.09	2.66×10^{-16}	6.09	2.53×10^{-16}	6.1	2.63×10^{-16}	6.88	4.86×10^{-18}	7.18	7.98×10^{-19}	6.1	2.63×10^{-16}	6.94	3.02×10^{-18}	6.84	5.95×10^{-18}	7.06	1.79×10^{-18}
6.4	3.76×10^{-17}	6.37	5.22×10^{-17}	6.36	6.85×10^{-17}	6.36	6.85×10^{-17}	7.14	1.10×10^{-18}	6.7	1.09×10^{-17}	6.94	7.98×10^{-19}	7.28	5.68×10^{-19}	7.28	5.68×10^{-19}
6.71	6.37×10^{-18}	6.66	1.37×10^{-17}	6.62	1.89×10^{-17}	6.62	1.89×10^{-17}	6.4	6.4×10^{-17}	6.4	6.4×10^{-17}	6.23	1.51×10^{-16}	6.18	2.29×10^{-16}	6.81	1.79×10^{-17}
7.02	1.56×10^{-18}	6.94	2.87×10^{-18}	6.88	4.86×10^{-18}	7.14	1.10×10^{-18}	6.7	1.09×10^{-17}	6.7	1.09×10^{-17}	7.18	7.98×10^{-19}	7.06	1.79×10^{-18}	6.62	1.99×10^{-17}
7.33	3.22×10^{-19}	7.22	4.72×10^{-19}	7.14	1.10×10^{-18}	7.93	1.46×10^{-20}	7.41	2.28×10^{-19}	7.14	1.10×10^{-18}	7.65	7.18×10^{-15}	7.5	1.82×10^{-19}	7.72	5.8×10^{-20}
7.64	4.47×10^{-20}	7.51	8.00×10^{-20}	7.4	2.44×10^{-19}	7.66	5.84×10^{-20}	7.41	2.28×10^{-19}	7.66	5.84×10^{-20}	7.89	2.20×10^{-20}	7.5	1.82×10^{-19}	7.94	1.87×10^{-20}
7.95	6.12×10^{-21}	7.79	1.60×10^{-20}	7.66	5.84×10^{-20}	7.93	1.46×10^{-20}	7.65	7.19×10^{-20}	7.89	5.56×10^{-21}	8.13	5.56×10^{-21}	8.16	5.68×10^{-21}	8.38	1.55×10^{-21}
8.26	9.22×10^{-22}	8.07	3.96×10^{-21}	7.93	1.46×10^{-20}	8.19	3.36×10^{-21}	8.45	7.29×10^{-22}	8.13	5.56×10^{-21}	8.37	1.28×10^{-21}	8.71	1.53×10^{-22}	8.72	5.8×10^{-20}
8.57	1.34×10^{-22}	8.35	9.64×10^{-22}	8.64	1.70×10^{-22}	8.45	7.29×10^{-22}	8.71	1.53×10^{-22}	8.13	5.56×10^{-21}	8.37	1.28×10^{-21}	8.71	1.53×10^{-22}	8.72	5.8×10^{-20}

TABLE VII. Logarithmic negativity as a function of separation measured in units of the averaged region diameter with an N-type boundary appearing in the left panel of Fig. 3.

$d_{lat} = 33$				$d_{lat} = 37$				$d_{lat} = 39$			
$d_{lat} = 31$		\tilde{r}/d_{avg}	\mathcal{N}	$d_{lat} = 35$		\tilde{r}/d_{avg}	\mathcal{N}	$d_{lat} = 37$		\tilde{r}/d_{avg}	\mathcal{N}
\tilde{r}/d_{avg}	\mathcal{N}	2.64	2.55×10^{-8}	\tilde{r}/d_{avg}	\mathcal{N}	2.62	2.79×10^{-8}	2.61	3.01×10^{-8}	\tilde{r}/d_{avg}	\mathcal{N}
2.63	2.66×10^{-8}	2.8	1.15×10^{-8}	2.63	2.64×10^{-8}	2.79	1.16×10^{-8}	2.77	1.26×10^{-8}		
2.8	1.19×10^{-8}	2.96	4.78×10^{-9}	2.81	1.06×10^{-8}	2.96	4.39×10^{-9}	2.93	4.92×10^{-9}		
2.97	4.92×10^{-9}	3.12	1.85×10^{-9}	2.99	3.85×10^{-9}	3.13	1.65×10^{-9}	3.09	2.00×10^{-9}		
3.14	1.82×10^{-9}	3.28	7.49×10^{-10}	3.17	1.36×10^{-9}	3.3	6.91×10^{-10}	3.26	8.91×10^{-10}		
3.31	6.67×10^{-10}	3.44	3.36×10^{-10}	3.35	5.30×10^{-10}	3.48	3.04×10^{-10}	3.42	4.13×10^{-10}		
3.48	2.73×10^{-10}	3.6	1.58×10^{-10}	3.53	2.21×10^{-10}	3.65	1.29×10^{-10}	3.58	1.85×10^{-10}		
3.65	1.22×10^{-10}	3.76	7.28×10^{-11}	3.71	9.00×10^{-11}	3.82	5.09×10^{-11}	3.74	7.77×10^{-11}		
3.82	5.47×10^{-11}	3.92	3.10×10^{-11}	3.89	3.41×10^{-11}	3.99	1.91×10^{-11}	3.9	3.11×10^{-11}		
3.99	2.28×10^{-11}	4.08	1.23×10^{-11}	4.07	1.21×10^{-11}	4.16	7.45×10^{-12}	4.06	1.29×10^{-11}		
4.16	8.64×10^{-12}	4.24	4.93×10^{-12}	4.26	4.44×10^{-12}	4.33	3.14×10^{-12}	4.22	5.75×10^{-12}		
4.33	3.22×10^{-12}	4.4	2.17×10^{-12}	4.44	1.81×10^{-12}	4.5	1.38×10^{-12}	4.39	2.64×10^{-12}		
4.5	1.33×10^{-12}	4.56	1.02×10^{-12}	4.62	7.51×10^{-13}	4.67	5.96×10^{-13}	4.71	4.98×10^{-13}		
4.67	5.97×10^{-13}	4.72	4.77×10^{-13}	4.8	2.98×10^{-13}	4.84	2.46×10^{-13}	4.87	2.03×10^{-13}		
4.84	2.64×10^{-13}	4.88	2.10×10^{-13}	4.98	1.13×10^{-13}	5.01	9.52×10^{-14}	5.03	8.17×10^{-14}		
5.01	1.08×10^{-13}	5.05	8.69×10^{-14}	5.16	4.10×10^{-14}	5.18	3.67×10^{-14}	5.19	3.46×10^{-14}		
5.18	4.11×10^{-14}	5.21	3.42×10^{-14}	5.34	1.53×10^{-14}	5.36	1.52×10^{-14}	5.35	1.55×10^{-14}		
5.36	1.49×10^{-14}	5.37	1.34×10^{-14}	5.52	6.01×10^{-15}	5.53	6.57×10^{-15}	5.52	7.04×10^{-15}		
5.53	5.50×10^{-15}	5.53	5.67×10^{-15}	5.7	2.41×10^{-15}	5.7	2.76×10^{-15}	5.68	3.08×10^{-15}		
5.7	2.29×10^{-15}	5.69	2.62×10^{-15}	5.89	9.52×10^{-16}	5.87	1.12×10^{-15}	5.84	1.31×10^{-15}		
5.87	1.02×10^{-15}	5.85	1.22×10^{-15}	6.07	3.73×10^{-16}	6.04	4.50×10^{-16}	6.	5.45×10^{-16}		
6.04	4.45×10^{-16}	6.01	5.39×10^{-16}	6.25	1.41×10^{-16}	6.21	1.77×10^{-16}	6.16	2.28×10^{-16}		
6.21	1.77×10^{-16}	6.17	2.25×10^{-16}	6.43	5.17×10^{-17}	6.38	6.96×10^{-17}	6.32	9.80×10^{-17}		
6.38	6.85×10^{-17}	6.33	9.31×10^{-17}	6.61	1.97×10^{-17}	6.55	2.84×10^{-17}	6.48	4.32×10^{-17}		
6.55	2.70×10^{-17}	6.49	3.91×10^{-17}	6.79	7.85×10^{-18}	6.72	1.19×10^{-17}	6.65	1.88×10^{-17}		
6.72	1.08×10^{-17}	6.65	1.67×10^{-17}	6.97	3.07×10^{-18}	6.89	4.93×10^{-18}	6.81	7.94×10^{-18}		
6.89	4.44×10^{-18}	6.81	7.22×10^{-18}	7.15	1.18×10^{-18}	7.06	2.02×10^{-18}	6.97	3.34×10^{-18}		
7.06	1.89×10^{-18}	6.97	3.12×10^{-18}	7.33	4.54×10^{-19}	7.24	8.30×10^{-19}	7.13	1.42×10^{-18}		
7.23	7.85×10^{-19}	7.13	1.32×10^{-18}	7.52	1.69×10^{-19}	7.41	3.34×10^{-19}	7.29	5.97×10^{-19}		
7.4	2.98×10^{-19}	7.29	5.53×10^{-19}	7.7	5.99×10^{-20}	7.58	1.30×10^{-19}	7.45	2.48×10^{-19}		
7.57	1.06×10^{-19}	7.46	2.27×10^{-19}	7.88	2.17×10^{-20}	7.75	5.14×10^{-20}	7.61	1.04×10^{-19}		
7.74	3.91×10^{-20}	7.62	9.33×10^{-20}	8.06	8.33×10^{-21}	7.92	2.13×10^{-20}	7.78	4.40×10^{-20}		
7.91	1.51×10^{-20}	7.78	3.93×10^{-20}	8.24	3.37×10^{-21}	8.09	9.06×10^{-21}	7.94	1.87×10^{-20}		
8.08	6.02×10^{-21}	7.94	1.69×10^{-20}	8.42	1.40×10^{-21}	8.26	3.84×10^{-21}	8.1	8.05×10^{-21}		
8.25	2.53×10^{-21}	8.1	7.37×10^{-21}			8.43	1.57×10^{-21}	8.26	3.48×10^{-21}		
8.43	1.10×10^{-21}	8.26	3.14×10^{-21}	8.42	1.28×10^{-21}						

TABLE VIII. Logarithmic negativity as a function of separation measured in units of the averaged region diameter with an N-type boundary appearing in the left panel of Fig. 3.

$d_{lat} = 41$				$d_{lat} = 43$				$d_{lat} = 47$				$d_{lat} = 49$			
\tilde{r}/d_{avg}	\mathcal{N}														
2.6	3.24×10^{-8}	2.61	3.00×10^{-8}	2.59	3.16×10^{-8}	3.27	4.57×10^{-9}	2.93	4.57×10^{-9}	2.76	1.15×10^{-8}	2.59	3.05×10^{-8}	2.76	1.15×10^{-8}
2.8	1.04×10^{-8}	2.8	9.93×10^{-9}	3.	3.29×10^{-9}	2.81	8.88×10^{-9}	3.44	3.54×10^{-10}	3.1	1.98×10^{-9}	3.27	8.64×10^{-10}	3.61	1.36×10^{-10}
3.01	3.20×10^{-9}	3.19	1.25×10^{-9}	3.39	4.92×10^{-10}	3.04	2.74×10^{-9}	3.48	2.98×10^{-10}	3.26	9.32×10^{-10}	3.78	5.31×10^{-11}	3.96	2.25×10^{-11}
3.21	1.13×10^{-9}	3.39	1.80×10^{-10}	3.77	5.94×10^{-11}	3.48	8.64×10^{-11}	3.7	8.64×10^{-11}	4.13	9.87×10^{-12}	4.16	4.16×10^{-12}	4.3	4.16×10^{-12}
3.41	4.28×10^{-10}	3.58	1.80×10^{-10}	3.97	2.04×10^{-11}	3.26	2.65×10^{-11}	4.14	9.03×10^{-12}	4.47	1.65×10^{-12}	4.64	6.37×10^{-13}	4.73	1.95×10^{-13}
3.62	1.51×10^{-10}	4.16	7.83×10^{-12}	4.36	3.04×10^{-12}	4.14	2.73×10^{-14}	4.59	8.58×10^{-13}	4.81	2.58×10^{-13}	5.15	4.75×10^{-14}	5.25	2.71×10^{-14}
3.82	4.76×10^{-11}	4.16	7.83×10^{-12}	4.55	1.09×10^{-12}	4.37	2.73×10^{-14}	5.14	4.65×10^{-14}	5.03	8.23×10^{-14}	5.32	1.95×10^{-14}	5.45	1.02×10^{-14}
4.02	1.55×10^{-11}	4.16	7.83×10^{-12}	4.55	1.09×10^{-12}	4.37	2.73×10^{-14}	5.14	4.65×10^{-14}	5.03	8.23×10^{-14}	5.49	7.73×10^{-15}	5.65	3.52×10^{-15}
4.23	5.74×10^{-12}	4.36	3.04×10^{-12}	4.75	3.64×10^{-13}	4.59	8.64×10^{-11}	5.53	1.79×10^{-14}	5.25	2.56×10^{-15}	5.66	2.99×10^{-15}	5.86	1.14×10^{-15}
4.43	2.16×10^{-12}	4.36	3.04×10^{-12}	4.75	3.64×10^{-13}	4.59	8.64×10^{-11}	5.53	6.46×10^{-15}	5.47	8.65×10^{-15}	5.83	1.21×10^{-15}	6.06	3.67×10^{-16}
4.63	7.38×10^{-13}	4.75	3.64×10^{-13}	5.14	1.24×10^{-13}	4.81	2.54×10^{-13}	5.72	2.21×10^{-15}	5.69	7.69×10^{-16}	6.	5.17×10^{-16}	6.26	1.27×10^{-16}
4.84	2.30×10^{-13}	4.94	1.24×10^{-13}	5.14	4.65×10^{-14}	4.81	2.54×10^{-13}	5.92	7.55×10^{-16}	5.92	2.50×10^{-16}	6.17	2.22×10^{-16}	6.47	4.65×10^{-17}
5.04	7.40×10^{-14}	5.14	4.65×10^{-14}	5.72	1.79×10^{-14}	5.25	2.73×10^{-14}	5.92	7.55×10^{-16}	5.69	2.50×10^{-17}	6.34	9.13×10^{-17}	6.67	1.63×10^{-17}
5.25	2.71×10^{-14}	5.14	4.65×10^{-14}	5.72	2.21×10^{-15}	5.69	2.50×10^{-17}	6.11	2.75×10^{-16}	6.14	7.72×10^{-18}	6.51	3.66×10^{-17}	6.88	5.37×10^{-18}
5.45	1.02×10^{-14}	5.33	1.79×10^{-14}	5.72	2.21×10^{-15}	5.69	7.72×10^{-18}	6.31	1.06×10^{-16}	6.36	2.33×10^{-18}	6.68	1.47×10^{-17}	7.08	1.78×10^{-18}
5.65	3.52×10^{-15}	5.53	6.46×10^{-15}	5.92	7.55×10^{-16}	5.92	7.39×10^{-19}	7.09	1.68×10^{-18}	7.25	7.39×10^{-19}	6.85	5.99×10^{-18}	7.28	6.05×10^{-19}
5.86	1.14×10^{-15}	5.92	7.55×10^{-16}	6.5	3.96×10^{-17}	6.58	2.44×10^{-19}	7.28	6.17×10^{-19}	7.47	2.44×10^{-19}	7.02	2.49×10^{-18}	7.49	2.09×10^{-19}
6.06	3.67×10^{-16}	6.11	2.75×10^{-16}	6.5	3.96×10^{-17}	6.58	2.44×10^{-19}	7.48	2.30×10^{-19}	7.69	7.77×10^{-20}	7.19	1.05×10^{-18}	7.69	7.12×10^{-20}
6.26	1.27×10^{-16}	6.31	1.06×10^{-16}	6.5	3.96×10^{-17}	6.58	2.44×10^{-19}	7.67	8.35×10^{-20}	7.91	2.37×10^{-20}	7.36	4.35×10^{-19}	7.89	2.33×10^{-20}
6.47	4.65×10^{-17}	6.31	1.06×10^{-16}	6.7	1.36×10^{-17}	6.8	7.72×10^{-18}	7.87	2.90×10^{-20}	8.13	7.10×10^{-21}	7.53	1.79×10^{-19}	8.1	7.48×10^{-21}
6.67	1.63×10^{-17}	6.5	3.96×10^{-17}	6.7	1.36×10^{-17}	6.8	7.72×10^{-18}	8.06	9.85×10^{-21}	8.26	3.46×10^{-21}	7.7	7.23×10^{-20}	8.3	2.54×10^{-21}

TABLE IX. Logarithmic negativity as a function of separation measured in units of the averaged region diameter with an N-type boundary appearing in the left panel of Fig. 3.

$d_{lat} = 57$		$d_{lat} = 67$		$d_{lat} = 79$	
\tilde{r}/d_{avg}	\mathcal{N}	\tilde{r}/d_{avg}	\mathcal{N}	\tilde{r}/d_{avg}	\mathcal{N}
2.58	3.22×10^{-8}	2.56	3.28×10^{-8}	2.55	3.54×10^{-8}
2.76	1.17×10^{-8}	2.75	1.26×10^{-8}	2.76	1.25×10^{-8}
2.94	4.71×10^{-9}	2.93	5.04×10^{-9}	2.96	4.26×10^{-9}
3.12	1.93×10^{-9}	3.12	1.93×10^{-9}	3.17	1.35×10^{-9}
3.3	7.43×10^{-10}	3.3	6.89×10^{-10}	3.38	4.46×10^{-10}
3.48	2.68×10^{-10}	3.49	2.54×10^{-10}	3.59	1.58×10^{-10}
3.66	1.01×10^{-10}	3.67	1.01×10^{-10}	3.79	5.38×10^{-11}
3.85	4.09×10^{-11}	3.85	4.00×10^{-11}	4.	1.72×10^{-11}
4.03	1.66×10^{-11}	4.04	1.49×10^{-11}	4.21	5.75×10^{-12}
4.21	6.31×10^{-12}	4.22	5.37×10^{-12}	4.42	2.04×10^{-12}
4.39	2.30×10^{-12}	4.41	2.05×10^{-12}	4.62	7.00×10^{-13}
4.57	8.73×10^{-13}	4.59	8.22×10^{-13}	4.83	2.25×10^{-13}
4.75	3.52×10^{-13}	4.78	3.21×10^{-13}	5.04	7.37×10^{-14}
4.93	1.42×10^{-13}	4.96	1.18×10^{-13}	5.24	2.59×10^{-14}
5.11	5.45×10^{-14}	5.14	4.27×10^{-14}	5.45	8.97×10^{-15}
5.3	2.02×10^{-14}	5.33	1.63×10^{-14}	5.66	2.96×10^{-15}
5.48	7.49×10^{-15}	5.51	6.49×10^{-15}	5.87	9.68×10^{-16}
5.66	2.96×10^{-15}	5.7	2.55×10^{-15}	6.07	3.31×10^{-16}
5.84	1.21×10^{-15}	5.88	9.57×10^{-16}	6.28	1.15×10^{-16}
6.02	4.81×10^{-16}	6.07	3.51×10^{-16}	6.49	3.94×10^{-17}
6.2	1.84×10^{-16}	6.25	1.32×10^{-16}	6.69	1.31×10^{-17}
6.38	6.89×10^{-17}	6.43	5.12×10^{-17}	6.8	4.32×10^{-18}
6.57	2.61×10^{-17}	6.62	1.99×10^{-17}	7.11	1.48×10^{-18}
6.75	1.02×10^{-17}	6.8	7.60×10^{-18}	7.32	5.05×10^{-19}
6.93	4.01×10^{-18}	6.99	2.87×10^{-18}	7.52	1.71×10^{-19}
7.11	1.55×10^{-18}	7.17	1.08×10^{-18}	7.73	5.63×10^{-20}
7.29	5.96×10^{-19}	7.36	4.13×10^{-19}	7.94	1.87×10^{-20}
7.47	2.25×10^{-19}	7.54	1.60×10^{-19}	8.14	6.35×10^{-21}
7.65	8.42×10^{-20}	7.72	6.14×10^{-20}		
7.84	3.25×10^{-20}	7.91	2.33×10^{-20}		
8.02	1.29×10^{-20}	8.09	8.66×10^{-21}		
8.2	5.11×10^{-21}				

TABLE X. Logarithmic negativity as a function of separation measured in units of the averaged region diameter with an N-type boundary appearing in the left panel of Fig. 3.

N boundary		S boundary		N boundary		S boundary	
$1/d_{lat}$	β_{2D}	$1/d_{lat}$	β_{2D}	$1/d_{avg}$	β_{2D}	$1/d_{avg}$	β_{2D}
$\frac{1}{21}$	5.955(80)	$\frac{1}{20}$	5.680(56)	0.052	5.428(63)	0.052	5.466(54)
$\frac{1}{23}$	5.908(61)	$\frac{1}{22}$	5.556(34)	0.047	5.410(70)	0.047	5.350(31)
$\frac{1}{25}$	5.823(40)	$\frac{1}{24}$	5.540(17)	0.044	5.308(32)	0.043	5.323(18)
$\frac{1}{27}$	5.698(26)	$\frac{1}{26}$	5.475(35)	0.04	5.310(25)	0.039	5.331(31)
$\frac{1}{29}$	5.633(17)	$\frac{1}{28}$	5.457(13)	0.037	5.278(17)	0.037	5.295(13)
$\frac{1}{31}$	5.628(23)	$\frac{1}{30}$	5.408(21)	0.034	5.307(23)	0.034	5.287(19)
$\frac{1}{33}$	5.598(16)	$\frac{1}{32}$	5.380(8)	0.032	5.271(17)	0.032	5.264(7)
$\frac{1}{35}$	5.574(13)	$\frac{1}{34}$	5.392(16)	0.03	5.270(13)	0.03	5.274(17)
$\frac{1}{37}$	5.530(10)	$\frac{1}{36}$	5.380(14)	0.028	5.249(11)	0.028	5.262(15)
$\frac{1}{39}$	5.514(11)	$\frac{1}{38}$	5.394(6)	0.027	5.251(12)	0.027	5.260(6)
$\frac{1}{41}$	5.494(15)	$\frac{1}{40}$	5.344(10)	0.025	5.253(14)	0.024	5.246(11)
$\frac{1}{43}$	5.497(12)	$\frac{1}{42}$	5.329(11)	0.024	5.244(12)	0.023	5.254(12)
$\frac{1}{47}$	5.459(10)	$\frac{1}{44}$	5.340(11)	0.022	5.240(10)	0.021	5.238(10)
$\frac{1}{49}$	5.460(8)	$\frac{1}{48}$	5.334(11)	0.021	5.237(9)	0.018	5.238(10)
$\frac{1}{57}$	5.419(7)	$\frac{1}{56}$	5.304(10)	0.018	5.241(8)	0.017	5.245(8)
$\frac{1}{67}$	5.392(6)	$\frac{1}{58}$	5.315(7)	0.015	5.240(7)	0.015	5.243(7)
$\frac{1}{79}$	5.367(6)	$\frac{1}{68}$	5.300(7)	0.013	5.247(6)	0.013	5.245(8)
		$\frac{1}{80}$	5.299(7)				

TABLE XI. Negativity decay constants, β_{2D} , extracted at finite region pixelation appearing in the middle two panels of Fig. 3.

d_{lat}	$\tilde{r}_{\mathcal{N}}/d_{lat}$	17	18.59	34	36.59	51	56.59	68	74.62	84	92.52	100	110.4
1	1.000	18	18.72	35	38.69	52	56.71	69	76.72	85	94.64	101	112.5
2	1.000	19	20.79	36	38.81	53	58.83	70	76.86	86	94.76	102	112.7
3	3.000	20	20.95	37	40.92	54	58.94	71	78.97	87	96.87	103	114.8
4	3.250	21	23.05	38	41.05	55	61.07	72	79.10	88	97.00	104	114.9
5	5.200	22	23.18	39	43.15	56	61.20	73	81.21	89	99.10	105	117.0
6	5.333	23	25.26	40	43.30	57	63.30	74	81.32	90	99.23	106	117.1
7	7.429	24	25.42	41	45.39	58	63.43	75	83.44	91	101.3	107	119.3
8	7.625	25	27.52	42	45.52	59	65.54	76	83.57	92	101.5	108	119.4
9	9.667	26	27.65	43	47.63	60	65.67	77	85.68	93	103.6	109	121.5
10	9.800	27	29.74	44	47.77	61	67.77	78	85.81	94	103.7	110	121.6
11	11.91	28	29.86	45	49.87	62	67.90	79	87.91	95	105.8	111	123.7
12	12.00	29	32.00	46	50.00	63	70.02	80	88.05	96	105.9	112	123.8
13	14.15	30	32.10	47	52.11	64	70.14	81	90.16	97	108.1	113	126.0
14	14.21	31	34.23	48	52.25	65	72.25	82	90.28	98	108.2	114	126.1
15	16.33	32	34.34	49	54.35	66	72.38	83	92.40	99	110.3	115	128.2
16	16.50	33	36.45	50	54.48	67	74.49						

TABLE XII. Entanglement bubble radii for regions of the one-dimensional massless scalar field appearing in the right panel of Fig. 3.

N boundary		S boundary (even)		S boundary (odd)	
d_{lat}	$\tilde{r}_{\mathcal{N}}/d_{lat}$	d_{lat}	$\tilde{r}_{\mathcal{N}}/d_{lat}$	d_{lat}	$\tilde{r}_{\mathcal{N}}/d_{lat}$
3	1.33	4	1.50	3	1.67
5	2.00	6	3.00	5	2.60
7	3.00	8	4.00	7	3.71
9	4.11	10	5.20	9	5.11
11	5.36	12	6.42	11	6.27
13	6.46	14	7.64	13	7.62
15	7.47	16	9.00	15	8.80
21	11.4	18	10.2	17	10.0
25	13.6				

TABLE XIII. Entanglement bubble radii for regions of the two-dimensional massless scalar field appearing in the right panel of Fig. 3.